



Mesoscale cortical mechanisms of perceptual conflict resolution in binocular rivalry

Received: 28 May 2024

Accepted: 10 September 2025

Published online: 13 November 2025

 Check for updates

Chencan Qian  ¹, **Zihao Zhang** ^{1,2,3}, **Zhiqiang Chen** ^{1,3,4}, **Gilles de Hollander** ^{5,6,7},
Tomas Knapen ^{6,7,8}, **Sheng He** ^{1,2,3} & **Peng Zhang**  ^{1,3} 

How does the human brain resolve conflicts in sensory input to generate conscious perception? Using high-resolution 7 T functional MRI, we addressed this question by investigating column- and layer-specific activity in cortical and subcortical regions in humans during binocular rivalry. The results show that eye-specific rivalry arises from interocular inhibition between adjacent ocular dominance columns in the superficial layers of the primary visual cortex, but not between ocular layers of the lateral geniculate nucleus of the thalamus. Eye-specific feedback from the intraparietal sulcus plays an active role in biasing and synchronizing local competitions in the primary visual cortex into perceptually coherent representations, even without awareness of eye-of-origin information. These findings reveal the mesoscale mechanisms of perceptual conflict resolution in humans: local conflicts in sensory input are resolved by inhibitory microcircuits in the sensory cortex, while feedback signals from the parietal attention network bias and integrate local competitions into unified conscious perception.

Two incompatible images presented to the two eyes compete for access to consciousness in a stochastic fashion. This illusion, called binocular rivalry, is an ideal model to study how our brains resolve conflicts in sensory input¹, a key mechanism to generate conscious perception^{2,3}. While previous neuroimaging studies have investigated large-scale activity at the level of brain areas⁴, mesoscale mechanisms of perceptual conflict resolution at the level of cortical columns and layers remain unexplored.

It has been proposed that binocular rivalry could arise from interocular or eye-based competition in the early visual areas⁵. As depicted in Fig. 1a(i), interocular competition could arise from interlaminar inhibition in the lateral geniculate nucleus (LGN) through interneurons with dendrites extending to the interlaminar zone and adjacent ocular layer^{6,7}. It could also occur between ocular dominance columns (ODCs) in the primary visual cortex (V1) via lateral inhibition through interneurons with long-range horizontal connections

(Fig. 1a(ii))⁸. In support of this eye competition hypothesis, human functional MRI (fMRI) studies have shown robust eye-specific modulations during binocular rivalry in the blind-spot area⁹, in ocular-biased voxels in V1 (ref. 10) and even in the LGN of the thalamus¹⁰. However, since these early fMRI studies did not resolve eye-specific activity from V1 ODCs or LGN ocular layers, interocular competition in these early visual areas still lacks conclusive evidence.

In contrast to the fMRI results, single-unit spiking activity showed no evidence of binocular rivalry in the LGN of awake monkeys¹¹ and a weak effect in V1 (refs. 12,13). Since blood-oxygenation-level-dependent (BOLD) signals can reflect synaptic activity¹⁴, one possible explanation for the discrepancy between single-unit and fMRI results is that intracortical processing and feedback modulations drive the rivalry dynamics in these early visual areas (Fig. 1a(iii))¹³, which may influence the temporal structure rather than the spike rate of neuronal output¹⁴. Eye-specific feedback in binocular rivalry has been suggested

¹State Key Laboratory of Cognitive Science and Mental Health, Institute of Biophysics, Chinese Academy of Sciences, Beijing, China. ²Anhui Province Key Laboratory of Biomedical Imaging and Intelligent Processing, Institute of Artificial Intelligence, Hefei Comprehensive National Science Center, Hefei, China. ³School of Life Sciences, University of Chinese Academy of Sciences, Beijing, China. ⁴Sino-Danish College, University of Chinese Academy of Sciences, Beijing, China. ⁵Zurich Center for Neuroeconomics, Department of Economics, University of Zurich, Zurich, Switzerland. ⁶Cognitive Psychology, Vrije Universiteit Amsterdam, Amsterdam, the Netherlands. ⁷Spinoza Centre for Neuroimaging, Royal Academy of Sciences, Amsterdam, the Netherlands. ⁸Netherlands Institute for Neuroscience, Royal Academy of Sciences, Amsterdam, the Netherlands. E-mail: zhangpeng@ibp.ac.cn

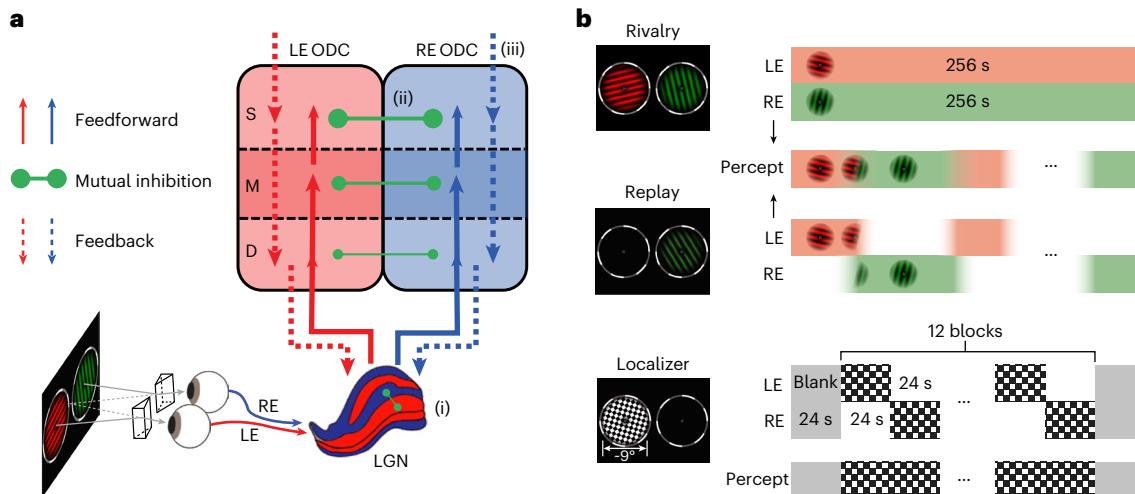


Fig. 1 | Candidate neural mechanisms and experimental design for studying interocular competition in binocular rivalry. **a**, Candidate mechanisms of interocular competition in binocular rivalry. (i) Interlaminar inhibition between ocular layers in the LGN. (ii) Intercolumnar inhibition between ODCs in V1. (iii) Eye-specific feedback modulation from higher-order brain areas. Solid and dashed arrows indicate feedforward and feedback connections, respectively. Green dots connected by solid green lines denote mutual inhibitions. Dot size

represents the strength of inhibition. S, superficial; M, middle; D, deep. **b**, Stimuli and procedures for the fMRI experiments. In rivalry runs, rotating red and green gratings in orthogonal orientations were dichoptically presented to the two eyes. In replay runs, monocular stimuli were alternatively presented to the two eyes to simulate the perception in the previous rivalry run. In localizer runs, a high-contrast flickering checkerboard was monocularly delivered to the two eyes in alternation.

by psychophysical evidence that top-down attention can modulate the duration of continuous flash suppression in an eye-specific fashion¹⁵, and by electrophysiological and neuroimaging studies showing that eye-specific representations can be found in extrastriate areas^{16,17}. In addition to eye-specific feedback, stimulus-pattern-based competition in the ventral stream could also interact with eye-based competition in the early visual areas^{18–20}.

An important source of feedback signals that might play critical roles in bi-stable perception is the frontoparietal cortex²¹. Previous human fMRI studies have primarily focused on content-agonistic activity around perceptual transitions in these high-order regions^{22–24}. However, the transition-related response can be largely eliminated when the perceptual switch is unreportable or invisible^{25,26}. Meanwhile, converging evidence shows that binocular rivalry requires top-down attention^{27,28}, suggesting a role of the frontoparietal attention network in resolving visual competition. Due to technical limitations in measuring weak and fine-scale representations in frontoparietal regions, perceptual state-related activity in these brain areas has not been reported in bi-stable perception in humans. Using a no-report paradigm based on eye movement, electrophysiological recordings in monkey prefrontal cortex revealed motion-related neural representations during binocular rivalry²⁹ and also suggested a causal role of low-frequency local field potentials in generating perceptual transitions³⁰. However, how frontoparietal regions interact with the early visual areas to generate conscious perception remains unclear. In addition, it remains unclear whether these high-order brain regions also play a role in eye-based competition along with the early visual areas. Feedback modulation from high-order brain regions could synchronize the dynamics of local competitions across space³¹, but this still lacks support from empirical neural evidence.

Therefore, although rivalry-related signals have been studied in multiple brain regions, it remains controversial whether eye-based competition initially occurs in V1 or in the LGN of the thalamus, and how feedback signals from high-order brain regions (in particular the frontoparietal areas) modulate local competitions in early visual areas. Using high-resolution 7 T fMRI in human participants, we investigated eye-specific signals in mesoscale functional units in cortical and subcortical regions during binocular rivalry and monocular replay simulation. Since the current study focused on the neural mechanism

of interocular competition, we did not analyse pattern-specific signals in these brain regions.

Results

Figure 1b shows the stimuli and procedures for the fMRI experiments. In the rivalry condition, a pair of red and green gratings were dichoptically presented in orthogonal orientations, rotating clockwise or counterclockwise to prolong the dominant duration of rivalry by reducing adaptation. Participants reported their perception using three buttons (red, green or mixed). The eye-colour associations (left eye (LE)–red/right eye (RE)–green, and vice versa) were swapped across runs. Thus, a percept was not bound to a particular eye, and we can isolate modulation with respect to eyes rather than stimulus colour. The dominant durations for the red and green gratings were approximately matched by adjusting luminance in a pilot experiment; thus, the dominant durations across eyes and stimuli were balanced during fMRI scans (Extended Data Fig. 1). In the replay condition, monocular red and green gratings were presented to the two eyes in alternation with simulated transitions to match the temporal sequence of perception during binocular rivalry. Participants reported their perception as in the rivalry condition. In localizer runs, a full-contrast counterphase flickering checkerboard was monocularly presented to the two eyes in alternation (without interleaving blank intervals) to measure the ocular bias of voxels. Continuous and prolonged stimulus presentation can stabilize the non-specific signals from large draining veins, thus increasing the spatial specificity of BOLD signals to enable functional mapping of mesoscale units such as cortical columns³², and was more robust to the superficial bias of BOLD signals (Extended Data Fig. 2).

In Experiment 1 (Exp. 1), we investigated eye-specific responses in different cortical depths of V1 ODCs using a gradient-echo (GE) echo-planar-imaging (EPI) sequence at submillimetre (0.8-mm isotropic) resolution³³. Details about the imaging parameters are provided in the Methods. Given the limited field of view of submillimetre fMRI and the important roles of the parietal and extrastriate areas in binocular rivalry, EPI slices were in oblique-coronal orientation to cover these regions (Fig. 2h, Exp. 1). In a representative participant, the columnar and laminar response in V1 was measured using a 2D passband balanced steady-state free procession (bSSFP) sequence with 0.5-mm in-plane resolution and 1.5-mm slice thickness (Fig. 2h, bSSFP). Compared with

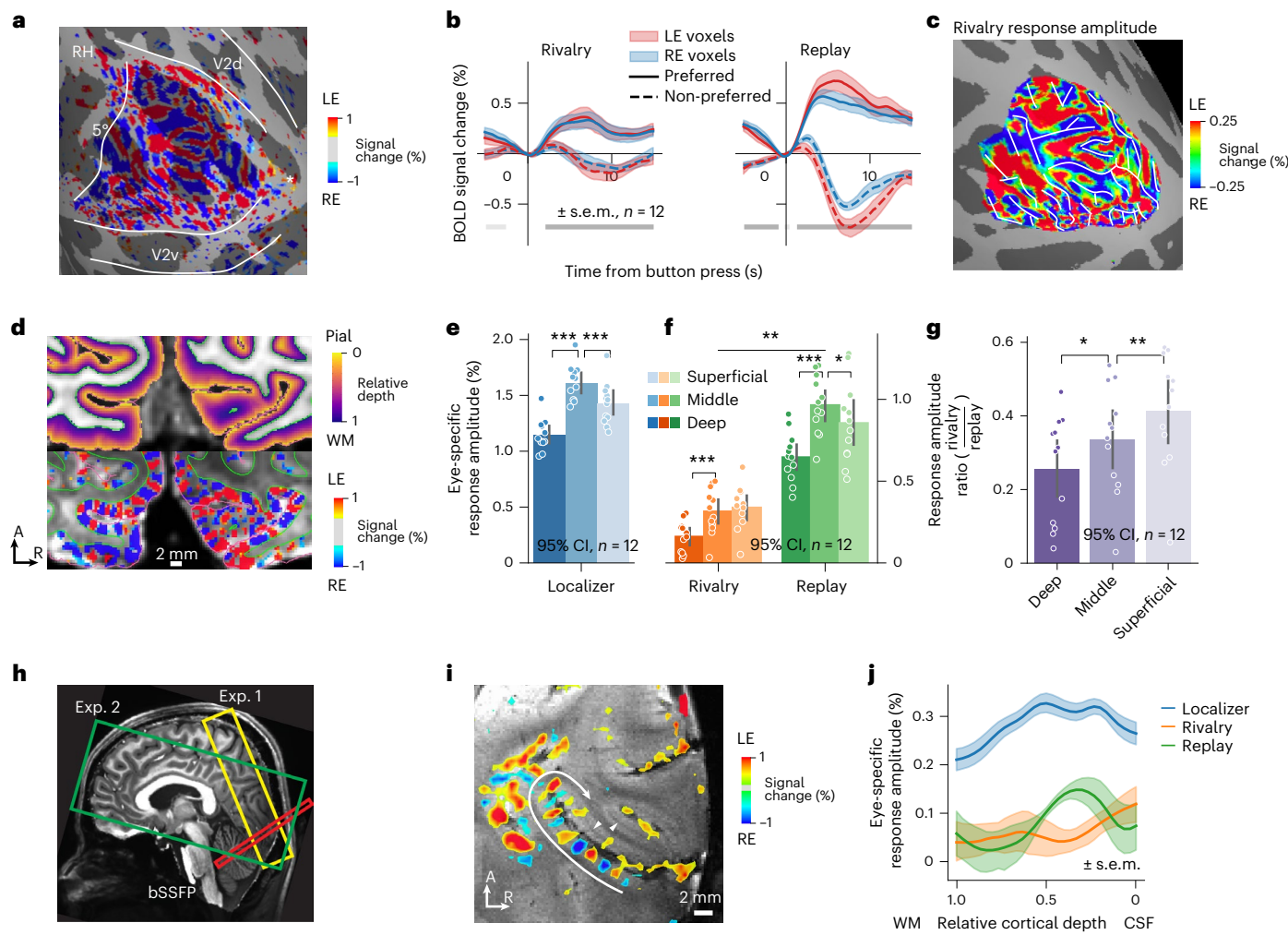


Fig. 2 | Eye-specific responses across cortical depth in V1 ODCs during binocular rivalry and replay (Exp. 1). **a.** ODC patterns on the inflated right hemisphere (RH) of a representative participant (S01, P.Z.). The colours represent the LE–RE BOLD per cent signal change ($P < 0.05$ uncorrected; two-sided t statistics). The white lines mark the V1/V2 boundaries and 5° eccentricity. **b.** Event-related eye-specific responses in ocular-biased voxels. The solid and dashed lines indicate responses to preferred and non-preferred percepts for the voxel. The grey bars denote significant differences (two-sided paired t -test, $P < 0.05$ uncorrected (light grey); or cluster-based permutation test, $P < 0.05$, family-wise error corrected (dark grey)). **c.** Eye-specific response pattern during rivalry (S01). The white lines outline RE-dominated columns (blue) in **a**. See Extended Data Fig. 3k for a side-by-side comparison. **d.** Top, equivolume cortical depth map (normalized depth) on a T1 image (S01). Bottom, LE–RE β map overlaid on mean EPI ($P < 0.05$ uncorrected; two-sided t statistics; only voxels in the grey matter are shown). Purple and green lines mark the pial and WM

surfaces. A, anterior; R, right. **e,f.** Depth profiles of eye-specific responses (preferred versus non-preferred) in localizer (blue) (**e**) and rivalry (orange) (**f**) and replay (green) (**f**). Two-sided paired t -tests were used for layer comparisons in **e–g**: * $P < 0.05$; ** $P < 0.01$; *** $P < 0.001$ (Holm corrected). **g.** Ratio of eye-specific responses during rivalry relative to replay. Depth effects were assessed via repeated-measures ANOVA ($F_{2,22} = 13.266$; $P < 0.001$; $\eta^2_G = 0.169$; 95% CI, (0.055, 0.432)). **h.** Coverage of EPI (Exp. 1 and 2) and bSSFP scans. **i.** ODC map (S06, C.Q.) on the cross section of the calcarine sulcus (white arrow) in the bSSFP experiment. The colours show the LE–RE per cent signal change ($P < 0.05$ uncorrected; two-sided t statistics). The T2*-weighted GRE overlay shows the line of Gennari. **j.** Laminar profiles of eye-specific responses in the bSSFP experiment. The bar plots in **e–g** show mean values with 95% CIs obtained by bootstrapping participants; individual data points are overlaid as dots. The line plots show mean values \pm s.e.m. across participants, except in **j**, where s.e.m. is computed across runs (13 localizer, 6 rivalry/replay).

GE-EPI BOLD, bSSFP fMRI signal is more sensitive to microvascular activity and thus has higher spatial specificity³⁴.

In Experiment 2 (Exp. 2), to further investigate whether the visual thalamus was involved in interocular competition during binocular rivalry, we examined ocular-layer-selective activity in the LGN using the same GE-EPI sequence at 1.2-mm isotropic resolution. Axial slices were orientated to cover the LGN, early visual cortices and the parietal cortex (Fig. 2h, Exp. 2). The stimuli and procedures were identical to those in Exp. 1.

Strongest rivalry modulation in the superficial layers of V1

Figure 2 shows the eye-specific response amplitude in V1 ODCs in Exp. 1. Interdigitated patterns of ODCs can be robustly detected in a

representative participant (S01, Fig. 2a; see Extended Data Fig. 3a,b for all participants), consistent with previous fMRI studies of human ODCs^{35–37}. The orientations of ODCs were roughly perpendicular to the V1/V2 border in its vicinity, and highly reproducible within (Extended Data Fig. 3c) and across scanning sessions (Extended Data Fig. 3d–f; $r = 0.697$, $P < 0.001$, Monte Carlo test). The ODC patterns were roughly consistent with cytochrome oxidase staining results in a postmortem study³⁸. The robust detection of ODCs is consistent with previous studies showing that the continuous stimulation paradigm can improve the spatial specificity of BOLD fMRI to map cortical columns^{32,39}. Eye-specific response time courses time-locked to the perceptual switch are shown in Fig. 2b. Following the perceptual switch, BOLD signals increased when the preferred stimulus was perceived (LE/RE

percept for LE/RE-biased voxels) and decreased when the non-preferred stimulus was perceived (RE/LE percept for LE/RE-biased voxels). The response amplitude in binocular rivalry was about 30–40% of that in monocular replay. The map of eye-specific responses in binocular rivalry (the differential responses between the LE and RE percepts) matched well with the ODC map in the localizer (Fig. 2c and Extended Data Fig. 3k,l; $r = 0.475$; $P < 0.001$; mean $r = 0.30$; 95% confidence interval (CI), (0.2, 0.39) in all participants; $t_{11} = 6.867$; $P < 0.001$; Cohen's $d = 1.982$). These results clearly demonstrate that eye-specific rivalry in V1 occurs at the level of ODCs.

To further investigate the laminar profile of eye-specific responses, we estimated cortical depth for each voxel using the equivolume algorithm⁴⁰, on the basis of manually edited cortical surface reconstructions (Fig. 2d, top). The columnar structure of ODCs perpendicular to the cortical surface can be clearly seen (Fig. 2d, bottom). The alignment and segmentation for all participants are shown in Extended Data Fig. 4a,b. Figure 2e illustrates the eye-specific response amplitude across cortical depth in the ocular bias localizer, defined as the BOLD response difference between the LE and RE stimulus conditions. The laminar response profile peaked in the middle depth of V1, consistent with the laminar pattern of thalamocortical projections mainly in layer 4C. This laminar pattern suggests that the differential approach with continuous stimulus presentation can help reduce non-specific signals from large veins⁴¹. More detailed demonstrations of the specificity of this method are shown in Extended Data Figs. 2 and 5b.

The shapes of laminar profiles showed a clear difference between rivalry and replay (Fig. 2f), demonstrated by a significant interaction between cortical depth (superficial/middle深深) and stimulus condition (rivalry/replay): $F_{2,22} = 7.209$; $P = 0.009$; $\eta^2_G = 0.049$; 95% CI, (0.029, 0.108) via bootstrapping participants. In the replay condition, the middle layer showed the strongest effect of eye-specific modulation (main effect of depth, $F_{2,22} = 25.695$; $P < 0.001$; $\eta^2_G = 0.332$; 95% CI, (0.237, 0.544); deep versus middle, $t_{11} = -11.084$; $P < 0.001$; $d = 1.937$; 95% CI, (-0.38, -0.26); middle versus superficial, $t_{11} = 2.667$; $P = 0.022$; $d = 0.509$; 95% CI, (0.02, 0.2); Bonferroni corrected). During binocular rivalry, eye-specific modulation was more biased toward the superficial depth (main effect of depth, $F_{2,22} = 26.094$; $P < 0.001$; $\eta^2_G = 0.306$; 95% CI, (0.141, 0.585); deep versus middle, $t_{11} = -5.485$; $P < 0.001$; $d = 1.291$; 95% CI, (-0.22, -0.09); middle versus superficial, $t_{11} = -1.196$; $P = 0.257$; $d = 0.173$; 95% CI, (-0.07, 0.02)). The eye-specific response change showed a large difference between the rivalry and replay conditions (Fig. 2f). Thus, to avoid the influence of mean response amplitude on the interaction effect, we normalized the eye-specific modulations by dividing the sum of responses across cortical depths in each stimulus condition. A significant depth-by-condition interaction could still be found following normalization ($F_{2,22} = 6.641$; $P = 0.013$; $\eta^2_G = 0.199$; 95% CI, (0.080, 0.460)). To further evaluate the difference in the shapes of the laminar profiles, we calculated a rivalry/replay response ratio for each cortical depth by dividing the response amplitudes in the rivalry condition by those in the replay condition. The rivalry/replay response ratio was strongest in the superficial layer (Fig. 2g; main effect of depth, $F_{2,22} = 13.266$; $P < 0.001$; $\eta^2_G = 0.169$; 95% CI, (0.055, 0.432); deep versus middle, $t_{11} = -2.835$; $P = 0.016$; $d = 0.547$; 95% CI, (-0.14, -0.02); middle versus superficial, $t_{11} = -3.186$; $P = 0.009$; $d = 0.515$; 95% CI, (-0.13, -0.02)).

One of the participants in Exp. 1 also participated in two additional sessions of the same experiment using the passband bSSFP sequence. Compared with GE-BOLD signals, passband bSSFP BOLD signals are more sensitive to microvascular activity in the grey matter and have higher spatial specificity to reveal layer-specific signals^{34,42}. Two coronal slices (0.5-mm in-plane resolution with 1.5-mm slice thickness) were carefully prescribed perpendicular to the calcarine sulcus in one hemisphere, where the ODCs went approximately parallel to the orientation of the anisotropic 'pencil' voxels (Fig. 2h and Extended Data Fig. 3g). One of the slices showed clear ODC patterns (Fig. 2i), confined within

the grey matter and highly reproducible across sessions (Extended Data Fig. 3h–j; $r = 0.757$, $P < 0.001$). The eye-specific response amplitude peaked in the middle cortical depth in monocular replay and ocular bias localizer, but was strongest in the superficial depth in binocular rivalry (Fig. 2j). This laminar pattern is consistent with the GE-BOLD results, providing additional evidence that in rivalry compared with replay, the peak of eye-specific modulation shifts towards the superficial layers of ODCs, consistent with local interocular competition in V1. We also tried to scan the 2D bSSFP sequence in other participants, including S01, who had the most robust OD pattern, but none of them were successful due to the difficulty in finding a location where the slices were perpendicular to both the cortical surface and the orientation of the cortical columns.

More synchronized rivalry dynamics in agranular layers of V1

Local interocular competition may result in different local winners and piecemeal perception. It has been hypothesized that feedback signals from higher-order areas help synchronize and stabilize local competitions into a globally coherent perceptual state over an extended visual field^{4,31}. To test this hypothesis, we characterized the synchronization of eye-specific modulations across V1 ODCs by calculating TR-by-TR Pearson correlations between the ongoing V1 response pattern and the localizer-derived OD pattern (Fig. 3a; TR, repetition time). More synchronized OD dynamics would predict correlation coefficients (r) away from zero, quantified by the width of the r distribution⁴³. In a simulation analysis (Extended Data Fig. 6a–f and Supplementary Methods), we showed that although the instantaneous correlation values themselves were small due to significant thermal noise in sub-millimetre fMRI, the r -distribution width can be sensitive to changes in synchronization and a small change in distribution width can reflect a measurable effect in synchronization. As stimulus-driven responses were fully coherent in the replay condition, this gave us a benchmark against which to compare the pattern coherence in the rivalry condition at each cortical depth. While the averaged response across columns (Fig. 2) may also capture the temporal synchronization of ODC responses, pattern correlation reflects not only the temporal synchronization but also the spatial homogeneities of suppression depth across the stimulus (Extended Data Fig. 6g,h), making it a more suitable metric in this analysis.

As predicted, we found that the replay condition was associated with a larger distribution width of correlation coefficients (Fig. 3b). Relative to replay, the superficial and deep layers of V1 in rivalry showed significantly larger distribution widths than the middle layer (Fig. 3c; main effect of depth, $F_{2,22} = 11.789$; $P < 0.001$; $\eta^2_G = 0.155$; 95% CI, (0.066, 0.361); deep versus middle, $t_{11} = 3.210$; $P = 0.008$; $d = 0.690$; 95% CI, (0.02, 0.12); middle versus superficial, $t_{11} = -4.789$; $P < 0.001$; $d = 0.942$; 95% CI, (-0.15, -0.06)). In addition to pattern synchronization, signal-to-noise ratio (SNR) may also strongly influence the r -distribution width. Thus, to investigate whether the superficial-and-deep laminar profile reflected a difference in signal synchronization or SNR, we performed a permutation analysis. A general linear model (GLM) was fitted to the time series of each vertex in the rivalry and replay conditions, using reported perceptual states as predictors. The fitted responses reflected the average eye-specific modulation, while the residuals represented noise variation including spatially synchronized activity that cannot be explained by the GLM. To remove synchronization while preserving noise, the residuals were temporally shuffled independently for each vertex and then recombined with the fitted time series. Pattern correlation with the new data showed no difference across cortical depth (Extended Data Fig. 6i). The permutation analysis thus supports a role of pattern synchronization rather than SNR in generating the laminar profile in Fig. 3c. By comparing our observation with the null distribution after noise shuffling, we confirmed that the deep layer had a larger rivalry/replay ratio of r -distribution width than the middle layer (Extended Data Fig. 6j; $P < 0.001$).

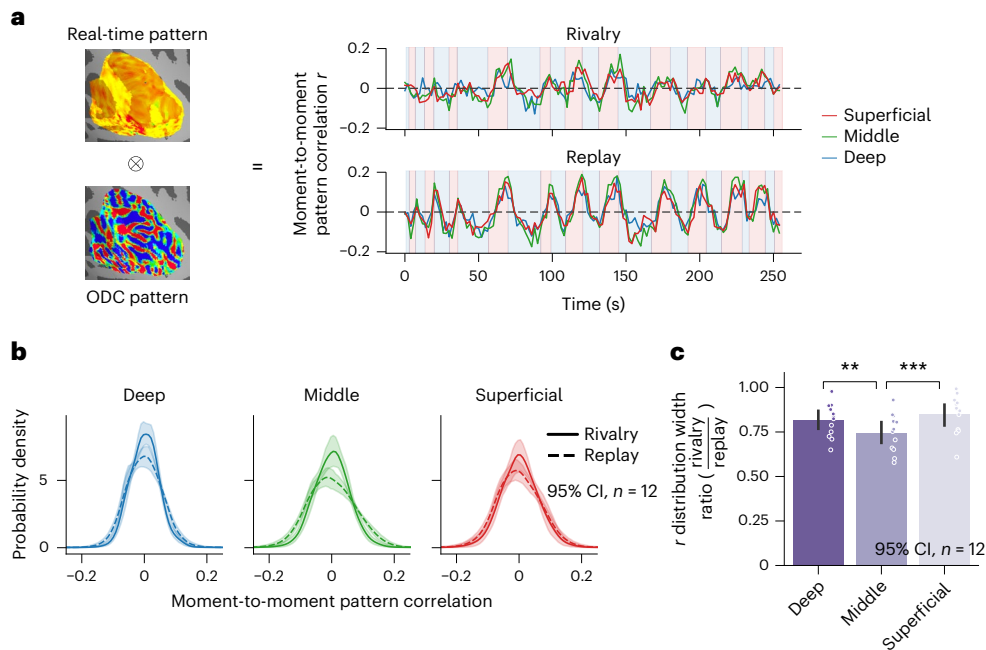


Fig. 3 | Pattern synchronization across ODCs in different cortical depths (Exp. 1). a, TR-by-TR Pearson correlations between the OD pattern from the localizer and the real-time V1 response pattern in typical runs of rivalry and replay. The data from a representative participant (S01) are shown. b, The distributions of pattern correlation (r) for different V1 layers in rivalry (solid) and replay (dashed). Red, green and blue lines indicate the results for the superficial, middle and deep layers, respectively. The shaded areas indicate 95% CIs across participants. c, The

ratio of r -distribution widths between rivalry and replay conditions across V1 layers. The main effect of depth was assessed via one-way repeated-measures ANOVA ($F_{2,22} = 11.789; P < 0.001; \eta^2_G = 0.155$; 95% CI, (0.066, 0.361)). Two-sided paired t -tests were performed to compare responses across layers. ** $P < 0.01$; *** $P < 0.001$; no correction needed for three levels given a significant main effect. The bar and line plots show mean values with 95% CIs obtained by bootstrapping participants; individual data points are overlaid as dots.

These results suggest that feedback processes were involved in synchronizing local competitions into a spatially coherent representation. To reveal the source of the feedback signals, we further examined eye-specific responses in the parietal and extrastriate visual cortices.

Eye-specific feedback from the intraparietal sulcus in binocular rivalry

The intraparietal sulcus (IPS) of the parietal cortex has been suggested to play a causal role in bi-stable perception in transcranial magnetic stimulation studies⁴⁴. Transition-related activity has been found in the IPS even in no-report paradigms^{24,45}. We thus examined whether the IPS encoded the eye-of-origin representation of the dominant stimulus, and its relationship with rivalry dynamics in V1. The univariate GLM analysis of localizer data did not show robust eye-specific activations in the IPS. Therefore, exploiting the sensitivity of multivariate methods, we trained a support vector machine (SVM) to predict the eye-of-origin of the stimulus. Feature selection was performed on the basis of the visual responsiveness and ocular bias of voxels in the localizer (Methods). The SVM was then used to predict the eye-of-origin of the perceived stimulus on a TR-by-TR basis during rivalry and replay. The distance between each activation pattern and the decision boundary of the SVM was used as a graded measure of the eye-specific representation (Fig. 4a,b). Event-related averages around the time of perceptual switches showed that, in the IPS, significant eye-specific modulation was observed in binocular rivalry but not in stimulus replay (Fig. 4c; cluster-based permutation test), similar in its posterior (pIPS, IPS0-2 in ref. 46) and anterior (aiIPS, IPS3-5) portions (condition \times region of interest (ROI) interaction not significant; $F_{1,11} = 0.115; P = 0.740; \eta^2_G = 0.001$; 95% CI, (0.0, 0.051)). Eye-specific modulation was also robust in extrastriate area V2 (similar to those in V1) and became weaker in V3 (Fig. 4d). In contrast to the early visual areas that showed significantly weaker modulation for rivalry than for replay, the IPS exhibited much stronger eye-specific modulation during binocular rivalry than during

replay ($t_{11} = 3.264; P = 0.015; d = 0.770$; 95% CI, (0.04, 0.23)). These findings suggest that the IPS might play an active role in binocular rivalry, for example by setting a competition bias to one eye. In the 1.2-mm dataset of Exp. 2 (8 of 15 participants had large coverage of the IPS), a significant eye-specific modulation was also found in the IPS during binocular rivalry but not stimulus replay (Extended Data Fig. 7a). In contrast, high-level visual areas in the ventral stream (hV4/VO) showed significant eye-specific modulation during replay, but the eye-specific effect was negligible during binocular rivalry.

The primary and extrastriate visual cortex and the frontoparietal cortex have been suggested to form a hierarchical network in binocular rivalry^{4,21}. We thus investigated the eye-specific information flow among V1, V2 and the IPS in a dynamic causal modelling (DCM) analysis. The multivariate projected time series that best discriminated LE from RE perception on the basis of an SVM trained on localizer runs was used. In the full DCM model (Fig. 4e, left), V1 receives eye-specific driving inputs in both the rivalry and replay conditions. Intrinsic or fixed connections were defined between and within cortical areas. The between-area connections as well as areas other than V1 could be modulated or driven by eye-specific input in rivalry but not in replay. This input thus captured the difference between the two conditions. The full DCM model was estimated for each individual. For group-level analysis, we used parametric empirical Bayes, Bayesian model reduction and Bayesian model average to make inferences about the model parameters. In rivalry compared with replay, feedback connections from the IPS to V2 and from V2 to V1 were significantly increased (connectivity change, 0.48 and 4.83 Hz, respectively; posterior probability >0.95 for both connections), whereas the feedforward connection from V1 to V2 significantly decreased (connectivity change, -0.60 Hz; posterior probability, 1.000). Although high-order visual areas in the ventral visual stream showed minimal eye-specific modulation during binocular rivalry, we further investigated the effective connectivity of eye-specific signals in a simplified global circuit model with V1,

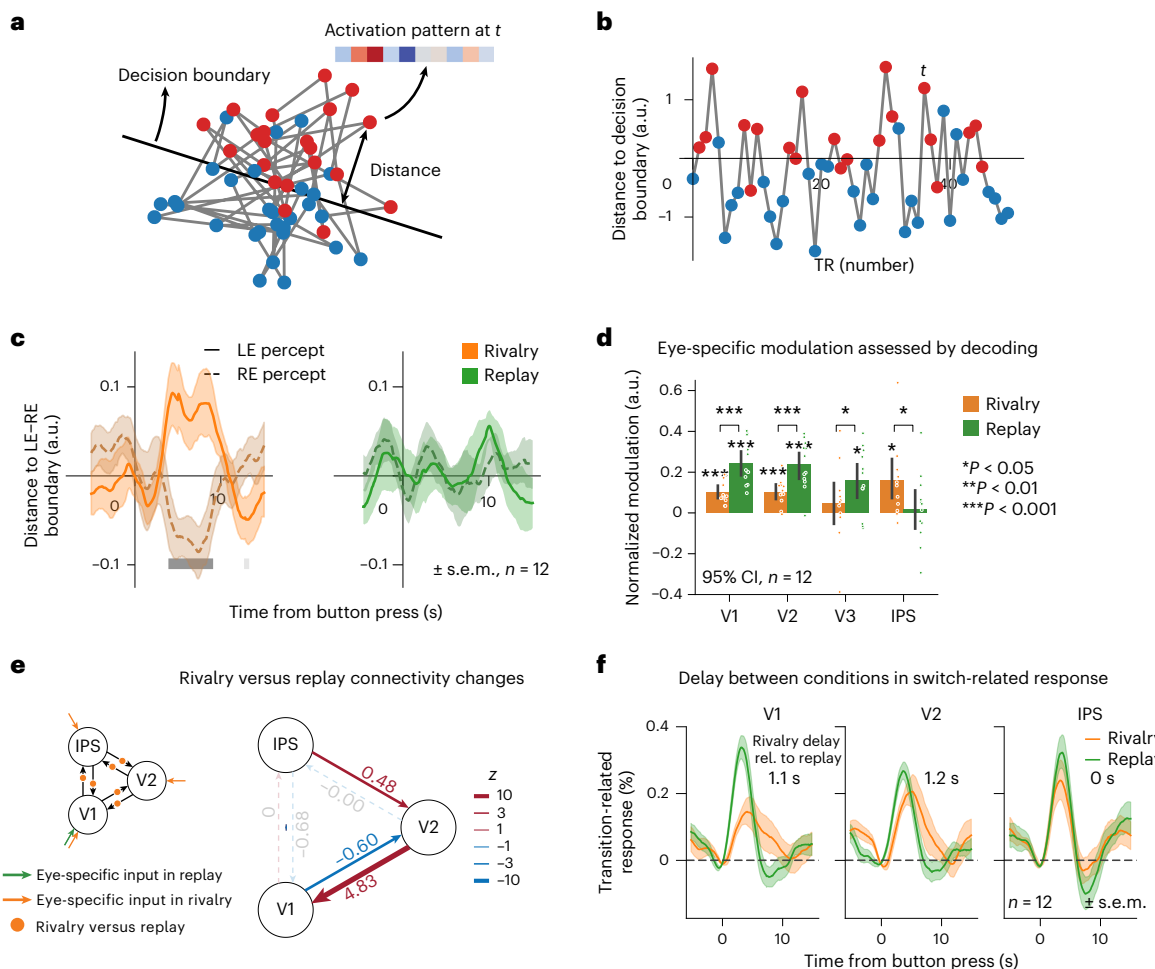


Fig. 4 | Eye-specific modulations in the IPS and its relationship with the early visual cortex (Exp. 1). **a**, Distance of the activation pattern at each time point to the SVM decision boundary for LE versus RE stimulation. Red (blue) dots denote the activation patterns of TRs when the LE (RE) was stimulated. **b**, The same distances replotted as a time course—that is, a multivariate differential response. **c**, Event-related average of the decoding-distance time course in the IPS for LE (solid) and RE (dashed) percepts in rivalry (orange) and replay (green). The shaded areas indicate s.e.m. The light and dark grey bars denote time points with significant differences between the two percepts before and after multiple testing correction. **d**, Eye-specific modulation in early visual areas and the IPS during rivalry and replay assessed by decoding. We applied one-sided one-sample t -tests to compare the modulation against zero and two-sided paired t -tests to compare between conditions (Holm corrected for multiple comparisons; for IPS, $t_{11} = 3.264$; $P = 0.015$; $d = 0.770$; 95% CI, (0.04, 0.23)). To facilitate the comparison between ROIs, the distance to the decision boundary

averaged between 4 and 12 s was normalized by dividing the L2-norm across participants and conditions for each ROI. **e**, Rivalry versus replay connectivity change among V1, V2 and the IPS. The numbers beside the connections denote the estimated modulatory effects in coupling strength (Hz), and the line thickness indicates the z value. Non-significant connections (posterior probability, <0.95) are plotted as low-contrast dashed lines. Left, DCM model specification for effective connectivity between the IPS, V2 and V1. V1 receives eye-specific driving input (green arrow) in the replay condition, while all three regions could receive eye-specific driving input (orange arrows) during binocular rivalry. The modulatory effect was defined as the connectivity difference between the rivalry and replay conditions (orange dots). **f**, Transition-related response ((LE + RE)/2 aligned to perception switch regardless of the dominant eye) in V1, V2 and the IPS. The delay of the transition response in rivalry (orange) relative to replay (green) was estimated using cross-correlation and annotated near the peaks.

hV4 and the IPS as the key brain regions (Extended Data Fig. 7b). The results support the idea that the feedback signal from the IPS is involved to modulate local interocular competitions in V1 during binocular rivalry.

In addition to eye-specific responses, we investigated non-eye-specific responses to perceptual transitions (irrespective of which eye's stimulus was perceived) (Fig. 4f). The results showed robust transition-related responses in both the rivalry and replay conditions. For the IPS, the response to perceptual transition in rivalry appeared roughly at the same time as in replay (cross-correlation delay, 0.0 s; 95% CI, (-0.5, 0.3) s; $P = 0.595$ by bootstrap). In contrast, the transition-related responses in rivalry were significantly delayed compared with those in replay in the early visual areas (1.1 s (0.1, 2.3) for V1, $P = 0.046$; and 1.2 s (0.3, 2.3) for V2, $P = 0.009$; Holm

corrected). The delay of rivalry transition relative to replay was significantly larger for V1 than for the IPS (delay difference, 1.1 s (0.3, 2.3), $P = 0.011$). Here, the difference in rivalry-to-replay delays cannot be attributed to the difference in haemodynamic function (HRF) delays across brain regions, because the replay response serves as a temporal reference and there was no significant delay even in the replay responses between V1 and the IPS (cross-correlation delay, 0.0 s (-0.3, 0.2), $P = 0.910$). Also, the delayed responses to rivalry transition in V1 and V2 were probably not due to delayed report or decision-making during rivalry, as there was no such delay in the IPS. Similar patterns were observed in the 1.2-mm dataset in Exp. 2 (Extended Data Fig. 7c). These findings provide additional evidence that the IPS may exert more top-down influence on the rivalry dynamics in V1 during binocular rivalry than during replay.

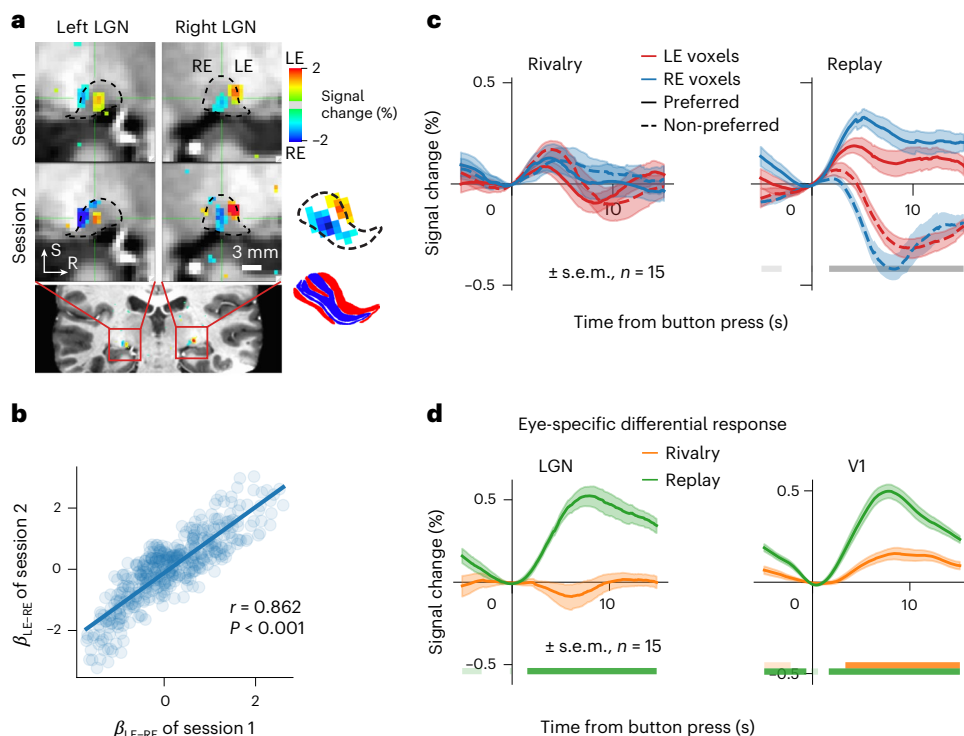


Fig. 5 | Eye-specific modulation in ocular-biased clusters of the LGN (Exp. 2).

a, Highly reproducible ocular-biased clusters in the LGN of a representative participant (S01, LE-RE β maps; $P < 0.01$, uncorrected; two-sided t statistics). ROIs were defined as visually responsive voxels in localizer runs in the first session (that is, LE + RE $P < 0.05$, uncorrected; two-sided t statistics). Voxels were upsampled to 0.6 mm isotropic resolution. The black dashed outlines indicate the boundary of the LGN, manually delineated by an experienced experimenter on T1-w anatomical images. See Extended Data Fig. 8 for ocular-biased clusters in the LGNs for all participants. Inset: simulation results of ocular-biased clusters.

b, Between-session correlation for the β values in the ocular-biased clusters in **a**, assessed using a Monte Carlo test to account for voxel non-independence.

c, Event-related average time courses for preferred and non-preferred percepts in the LGN ocular-biased clusters. **d**, Eye-specific modulation time courses in the LGN and V1 during rivalry and replay. The horizontal bars in light and dark colours denote time points with significant differences from zero for the corresponding conditions before and after multiple testing correction, respectively. Insets of panel **a** adapted with permission from ref. 47, Royal Society Publishing.

No evidence for eye-specific rivalry signals in the LGN

In Exp. 2, we further investigated whether the LGN of the thalamus was involved in interocular competition during binocular rivalry. Due to its small size and deep location in the middle of the brain, the LGN has much lower SNR than the visual cortex. Thus, to optimize the balance between spatial resolution and SNR for imaging ocular-biased activity in the LGN, we used a larger voxel at 1.2-mm isotropic resolution and less parallel imaging (an acceleration factor (R) of 2) than in Exp. 1 (0.8-mm isotropic voxels and $R = 3$). Robust ocular-biased patterns were clearly and consistently revealed in the LGN across sessions on separate days by the ocular bias localizer (Fig. 5a,b for S01; $r = 0.862$, $P < 0.001$, Monte Carlo test; see Extended Data Fig. 8 for the ocular bias patterns for all participants). There are two ocular-biased clusters for each LGN: a ventromedial one biased to the ipsilateral eye and a dorsolateral one biased to the contralateral eye, which replicated the findings of our recent study⁴⁷. According to the simulation analysis of the previous study, these ocular-biased clusters reflect a low-resolution laminar pattern of the LGN, resulting from the blurring effect of BOLD point spread function and the down-sampling effect of fMRI (reproduced here in the lower right of Fig. 5a). BOLD signals from the ocular-biased clusters therefore represent ocular-layer-selective activity of the LGN. For more details about the simulation analysis, please refer to Figs. 1b and 3a in our previous study⁴⁷.

To our surprise, although BOLD signals in ocular-biased clusters of the LGN showed a transient increase following perceptual switch (Fig. 5c; mean response to both preferred and non-preferred switches averaged between 2 and 6 s; $t_{14} = 4.112$; $P = 0.001$; $d = 1.062$; 95% CI, (0.05, 0.15)), there was no significant eye-specific modulation during

binocular rivalry (Fig. 5d; $t_{14} = -0.619$; $P = 0.546$; $d = 0.160$; 95% CI, (-0.08, 0.04); $BF_{01} = 3.226$, moderate evidence ($3 < BF_{01} < 10$) for the null hypothesis). As positive controls, the differential response to preferred and non-preferred eye stimulation averaged between 4 and 12 s was as strong in the LGN as in V1 in the replay condition, and V1 showed robust eye-specific modulations in both conditions (Fig. 5d). Although there was no evidence of eye-specific rivalry modulation in most-biased voxels in the ocular-biased clusters, a negative eye-specific effect was observed outside the ocular-biased clusters and a weaker effect in least-biased voxels inside the clusters (probably due to the partial volume effect) (Extended Data Fig. 9a,b). This negative effect could be due to attentional suppression outside the stimulus region^{48,49}. Since the pulvinar of the thalamus is located very close to the LGN, we analysed the pulvinar response to assess its potential contamination of the LGN signal. There was no significant eye-specific response in the rivalry or replay condition in the pulvinar (multivariate response amplitude in rivalry: $t_{14} = 1.504$; $P = 0.155$; $d = 0.388$; 95% CI, (-0.0, 0.03); and in replay: $t_{14} = 0.167$; $P = 0.870$; $d = 0.043$; 95% CI, (-0.01, 0.01)). Thus, the LGN results were probably not contaminated by the pulvinar signal.

Our 7 T fMRI results therefore suggest weak, if any, eye-specific rivalry modulation within the stimulus regions of the LGN. This finding is consistent with the single-unit study in awake macaques¹¹ and also with the observation in Exp. 1 that eye-specific rivalry modulation peaked in the superficial layers of V1. If interocular competition occurred in the LGN, one would expect a peak of eye-specific signals in the middle layer of V1 that mainly receives thalamic input. Although our data showed negligible eye-specific response in binocular rivalry, it remains possible that cortical feedback can modulate LGN activity in

a perception-related manner. In support of this, LGN activity has been found to correlate with contrast perception during binocular rivalry⁵⁰.

Discussion

Using high-resolution 7 T fMRI in humans, we investigated mesoscale neural dynamics in key brain regions during binocular rivalry and monocular replay. Compared with replay, eye-specific signal modulation in rivalry was strongest in the superficial layers of V1 ODCs and more synchronized in the superficial and deep layers. The IPS generated stronger eye-specific modulation and higher eye-specific feedback connectivity to V1 during rivalry than during replay. The transition-related response in the IPS also preceded those in the early visual areas. Finally, ocular-layer-selective activity in the LGN showed no evidence of eye-specific modulation during binocular rivalry. These findings provide important mesoscale evidence for the neural mechanisms of interocular competition in binocular rivalry.

In the localizer (Fig. 2e) and replay conditions (Fig. 2f), the eye-specific response amplitude was strongest in the middle cortical depth of V1, consistent with feedforward input from the LGN (Fig. 1a)⁵¹. Compared with replay, eye-specific response was biased towards the superficial depth of V1 in rivalry (Fig. 2f,g). This laminar pattern is consistent with local processing, or lateral inhibition between ODCs. Converging neuroanatomical and electrophysiological evidence supports this explanation. Anatomically, axon boutons of interneurons with long-range horizontal connections, the large basket cells and Martinotti cells^{8,52}, are mainly located in the superficial layers of the sensory cortex^{53–55}. Large basket cells spanning ODCs have also been found in layer 3 of cat V1 (ref. 56). Excitatory pyramidal cells have long-range horizontal connections mainly in the superficial layers of the early visual cortex^{57–59}. Electrophysiological evidence has shown that intercolumnar inhibition by horizontal connections was most pronounced in the superficial layers⁶⁰. Most importantly, dichoptic cross-orientation suppression has been found to be strongest in the superficial layers of V1 (refs. 61,62). This neuroanatomical and electrophysiological evidence suggests that intercolumnar inhibition between ODCs should be strongest in the superficial layers of V1, which is consistent with our laminar results in binocular rivalry. Thus, together with the weak or absent eye-specific rivalry signal in the LGN (Fig. 5d), our data support the idea that binocular rivalry arises from local interocular competition between ODCs in V1 by lateral inhibition. Rivalry signal in the superficial layers of V1 was probably not driven by long-range pulvino-cortical feedback targeting the superficial layers⁶³, as we found no evidence for eye-specific signal in the pulvinar. Although we cannot completely rule out possible feedback signals biased to the superficial layers, pattern correlation analysis revealed a distinct laminar profile for feedback modulation.

In addition to the laminar difference in response amplitude, eye-specific rivalry dynamics was more spatially synchronized in the deep and superficial depths of V1 (Fig. 3c), suggesting that feedback modulations from higher cortex are involved in synchronizing local competitions into perceptually coherent representations³¹. These layer-specific results could explain the discrepancy between single-unit and local field potential/fMRI results regarding perceptual suppression: the robust effect of perceptual suppression in fMRI signals reflects intracortical processing and feedback modulation of synaptic input¹³, which might influence the timing rather than the firing rate of neuronal output. It has also been proposed that perceptual rivalry might modulate both inhibitory and excitatory neural activity in balance¹³, leaving the spike rate unchanged but causing significant BOLD modulation. However, this is less likely to explain the eye-specific modulation in our results for the following reasons. First, almost 90% of neurons in the mammalian cortex are excitatory⁶⁴, and their activity accounts for the majority of energy consumption for neural signalling⁶⁵. Moreover, a recent study indicated that prolonged optogenetic stimulation of cortical interneurons reduced the excitatory neural

activity and BOLD signals at the stimulation site⁶⁶. Therefore, during the continuous stimulus presentation of binocular rivalry, the eye-specific BOLD modulation in V1 should mainly reflect changes in excitatory neural activity, probably a result of local interocular inhibition or top-down modulation.

Although robust ocular-layer-selective activity was observed in the LGN during both the localizer (Fig. 5a and Extended Data Fig. 8) and replay conditions (Fig. 5c,d), we found no evidence for eye-specific modulation during binocular rivalry. Thus, while binocular suppression occurs in the primate LGN^{67,68}, binocular rivalry does not appear to strongly modulate eye-specific activity in the ocular layers. This finding aligns with electrophysiological evidence showing no effect of binocular rivalry on LGN spike rates in awake monkeys¹¹. In contrast, previous 3 T fMRI studies in humans reported significant eye-specific effects of binocular rivalry in ocular-biased voxels of the LGN^{10,69}, although the more recent study showed limited consistency across a small number of participants⁶⁹. Several methodological factors probably account for this discrepancy. First, our negative finding is probably not due to the lack of power. Collected using 7 T fMRI with a smaller voxel size (1.2 mm versus 1.5 mm) and a larger sample size (15 versus 3–4 participants), our data have better sensitivity to detect eye-specific signals in the LGN. Another important difference is the stimulus size: prior studies employed larger stimuli (120° bilateral wedges between 1.5 and 7.5° eccentricity or 6.25° radius disc) than the current study (4.5° radius disc). Given that attention strongly modulates LGN activity⁷⁰ and that the temporal–nasal asymmetry of the attention effect is more pronounced in the peripheral visual field⁷¹, the reported eye-specific effects could reflect a difference in attentional modulation when participants perceived the temporal versus the nasal stimuli. Supporting this interpretation, we also found an eye-specific suppression effect outside the ocular-biased clusters (Extended Data Fig. 9a,b), probably due to attentional suppression outside the stimulus region⁴⁸. Finally, although we found no evidence for eye-specific rivalry modulation, overall LGN activity could still be influenced by non-eye-specific feedback associated with conscious perception. Our finding thus does not contradict another human fMRI study demonstrating that overall LGN activity tracks contrast perception during rivalry between low- and high-contrast gratings⁵⁰. While it remains possible that eye-specific rivalry signals exist in the LGN but were simply too weak to be detected by our methods, our results show that interlaminar inhibition in the LGN is unlikely to drive interocular competition in binocular rivalry.

The role of frontal and parietal association cortices in consciousness and bi-stable perception has been a subject of intense debate. Previous research focused on the causal relationship between perceptual-switch-related activity in frontoparietal areas and perceptual transitions²¹. In our study, perceptual-switch-related activity in the IPS precedes that in the early visual areas (V1/V2) during binocular rivalry when simulated replay is used as a temporal benchmark (Fig. 4f and Extended Data Fig. 7c). This finding is consistent with a recent electrophysiological study in human occipitotemporal cortex⁷². Taken together, these findings suggest that the IPS and high-level visual cortex may exert top-down influence on the rivalry dynamics in the early visual areas. More importantly, our data revealed significant eye-specific signal in the IPS during rivalry but not during replay (Fig. 4c,d and Extended Data Fig. 7a). The IPS also showed stronger eye-specific feedback connectivity to the early visual cortex during rivalry than during replay (Fig. 4e and Extended Data Fig. 7b). These findings strongly support the idea that the IPS is involved in interocular competition during binocular rivalry. Together with the more synchronized eye-specific rivalry dynamics in the superficial and deep layers of V1 (Fig. 3c), our data suggest that the IPS, in addition to the ventral stream areas, is involved in synchronizing local competitions into perceptually coherent representations. Given the important role of the IPS in attention and that participants were not aware of the eye-of-origin information, our findings are also consistent with previous studies showing that

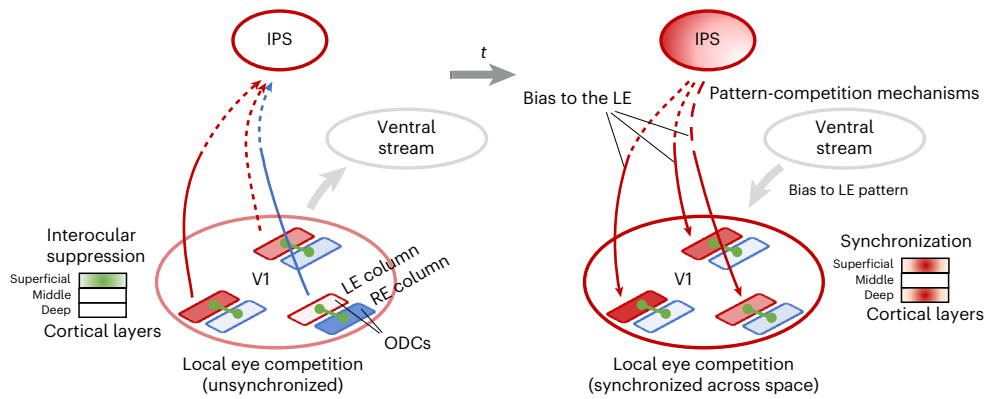


Fig. 6 | A hierarchical model for interocular conflict resolution in binocular rivalry. Local interocular competitions arise from the superficial layers of V1, synchronized by top-down modulation from IPS into a spatially coherent perceptual representation. Detailed descriptions are provided in the last paragraph in ‘Discussion’.

binocular rivalry requires attention^{27,28} but not awareness of conflicting information^{26,73}. Since the eye-of-origin classifier was trained on data in the localizer runs in which participants performed a central fixation task, the eye-specific effect in the IPS in rivalry and replay was probably not due to active reports of perception. Finally, the eye decoding in the IPS was probably not influenced by stimulus pattern information, because the same checkerboard stimulus was presented to the two eyes in the localizer to train the eye-of-origin classifiers, which were used to estimate the eye-specific signals to very different stimuli (red/green gratings) in rivalry and replay.

Although we found negligible eye-specific modulation in the ventral stream during binocular rivalry (Extended Data Fig. 7a), feedback signals from these high-level visual areas could also be involved in synchronizing the rivalry dynamics via pattern competition^{18,31,74}. Pattern competition could also occur in the IPS. Thus, while the mechanisms of interocular competition probably explain the bulk of binocular rivalry phenomena, a complex interplay between eye and pattern competitions would more fully determine the rivalry dynamics of conscious perception. Future high-resolution fMRI studies should investigate the stimulus-pattern-specific response and connectivity over the whole brain to more comprehensively understand the neural mechanisms of binocular rivalry. The eye-specific modulation observed in this study probably reflects the result of interocular competition rather than the more transient conflict-resolution process in the transition period due to the limited temporal resolution of fMRI signals. In addition, the predictions from the mesoscale neural circuitry model based on our fMRI results will need to be tested by future behavioural and electrophysiological studies.

It is known that the spatial specificity of T2*w BOLD signal is limited by its high sensitivity to large veins⁷⁵. To improve column and layer specificity, we combined several approaches to enhance the microvascular contribution to the BOLD signal. First, voxels influenced by large pial veins were excluded in a column-wise manner, which significantly reduced the superficial bias of the BOLD laminar profile (Extended Data Fig. 2a). Second, macrovascular activity shared by adjacent columns was suppressed by the differential approach, which improved the laminar specificity of column-specific signals (Extended Data Figs. 2 and 5a). Third, continuous stimulus presentation stabilized the macrovascular activity into a steady state, further improving the signal-to-noise ratio of microvascular activity. Fourth, the laminar profile of rivalry modulation was contrasted with perceptually matched replay simulation; thus, the resulting difference could not be easily explained by a common draining vein effect. Finally, bSSFP data from a representative participant with high microvascular sensitivity and specificity⁷⁶ provided at least a proof-of-concept replication of the GE-BOLD results. Robust ocular dominance responses peaked in the middle layers of V1, demonstrating the effectiveness of these approaches. As further evidence

for the high specificity of our 7 T data, the rivalry/replay modulation ratio is about 30–40% (Figs. 2b and 5d), close to the neural effect of perceptual suppression on low-frequency local field potentials (36%¹³). In contrast, the BOLD effect of binocular rivalry was much larger at lower magnetic fields (4.7 T, 72%¹³; 1.5 T, ~90%⁹), probably due to the nonlinearity of BOLD signals in large veins⁴².

Our results reconcile the long-standing discrepancy between monkey electrophysiology and human fMRI studies: perceptual modulations in the early visual areas mainly reflect local processing and feedback modulation of synaptic input, which lead to BOLD signal changes but not necessarily the spike rate of neuronal output. These findings provide important mesoscale evidence for a hierarchical model of eye-based competition in binocular rivalry (Fig. 6). When two incompatible images are presented to the two eyes, local interocular competitions arise between adjacent ODCs in the superficial layers of V1, initially unsynchronized across different locations. The interocular conflict signals are detected by and integrated in higher cortex, including the IPS, which sends feedback signals to bias and synchronize local competitions into more spatially coherent perceptual representation.

Methods

Participants

Sixteen healthy volunteers (seven females, aged 22–40 years) participated in Exp. 1. Three of them were excluded due to the lack of a clear OD pattern in V1, and one participant was excluded due to strong bias towards one eye. Fifteen participants (seven females, aged 22–39 years) participated in Exp. 2. All participants had normal or corrected-to-normal vision and provided written informed consent. Experimental protocols were approved by the Institutional Review Panel at the Institute of Biophysics, Chinese Academy of Sciences (Ethic No. 2012-IRB-011).

Stimuli and procedures

For the ocular bias localizer, to selectively activate V1 ODCs and LGN ocular layers, a high-contrast checkerboard (1° check size, 8–10° in diameter adjusted for each individual) counterphase flickering at 8 Hz was monocularly delivered to the LE or RE in alternating 24-s blocks. Two 24-s fixation blocks were included at the beginning and the end of the run. The checkerboard rotated at 3.75° per second. The stimuli were dichoptically presented with prisms and a cardboard divider. Participants reported occasional fixation-size changes. During binocular rivalry, red and green gratings (0.8 cycles per degree) in orthogonal orientations were dichoptically presented to the two eyes, rotating together at 0.67 rounds per second. The association between colour and eye swapped between runs. Participants reported whether they were seeing red, green or a mixed percept. In replay runs, the perception and timing of the previous rivalry run were simulated

with alternating monocular stimuli. The transition was simulated as a blurred and blended boundary rotating and swiping across the stimulus. Each rivalry or replay run lasted 256 s, whereas the localizer run lasted 336 s. Participants completed four to six localizer runs, four rivalry runs and four replay runs in a single session. For the bSSFP scans (S06), six localizer and six rivalry runs were collected in one session, followed by six localizer and six replay runs in another session.

MRI data acquisition

MRI data were acquired with a 7 T scanner (Siemens Magnetom) using a 32-channel receive single-channel transmit head coil (NOVA medical) in the Beijing MRI Center for Brain Research. A bite bar was used to reduce head motion. In Exp. 1, T2*w BOLD signals from the occipital and parietal cortices were acquired with a 2D GE-EPI sequence (0.8-mm isotropic voxels, TE = 23 ms, TR = 2,000 ms, 31 oblique-coronal slices). C.Q. was also scanned with a 2D passband bSSFP sequence (voxel size, $0.5 \times 0.5 \times 1.5 \text{ mm}^3$; 2 oblique-coronal slices; volume acquisition time, 3,200 ms). In Exp. 2, functional images were acquired with a 2D GE-EPI sequence (1.2-mm isotropic voxels, TE = 22 ms, TR = 2,000 ms, 31 (7 participants) or 62 (8 participants) axial slices). In all scanning sessions, full-brain anatomical images were acquired using a T1w MP2RAGE sequence (0.7-mm isotropic voxels). More details about the MRI parameters are presented in the Supplementary Methods.

MRI data analysis

Preprocessing. The MRI data were preprocessed using AFNI, FreeSurfer (v.6.0), ANTs and the mripy package (<https://github.com/herrich10/mripy>). EPI volumes were corrected for slice timing, distortion (blip-up/down) and head motion (rigid body) and scaled to per cent signal change. To minimize spatial resolution loss, all spatial transformations were combined and applied in a single interpolation (sinc method), in which the data were also up-sampled by a factor of 2. The anatomical volume and the reconstructed surfaces were aligned to the mean EPI. Baseline drift and motion parameters were included in the GLM and regressed out in time-course analyses. A canonical HRF (BLOCK4 in AFNI) was used. For the bSSFP data, motion correction was performed in-plane with in-plane rotation and translation. To alleviate bias induced by pial veins in laminar analysis, surface vertices with high signal change (mean stimulus-driven response over 10% in localizer runs) or low EPI intensity (below 75% of the mean EPI intensity) were classified as large veins⁷, and the corresponding columns of voxels were excluded from further analysis. A total of 38.8% (mean) \pm 12.5% (s.d.) of V1 vertices were excluded.

Surface segmentation and depth analysis. The anatomical volume was segmented into white matter (WM), grey matter and cerebrospinal fluid using FreeSurfer with the hires option. The initial segmentation results were visually inspected and manually edited to eliminate dura matter, sinus and so on, ensuring correct grey matter boundaries. To match the up-sampled volume grid and alleviate the vertex-missing problem during surface-to-volume projection, high-density surface meshes were created by subdividing each triangular face into 16 smaller ones at the quadrisection points of each edge.

The relative cortical depth for each voxel was estimated using the equivolume method⁴⁰. The neighbourhood area for a surface vertex was approximated by summing up the areas of surrounding triangular meshes. A set of intermediate surfaces at specified equivolume depths were then generated. Finally, the depth of the voxel centre was computed by interpolating between the two nearest iso-depth surfaces. The pial (WM) surface was defined to have a relative cortical depth of zero (one).

In GE-EPI analysis, the deep, middle and superficial layers were defined to take up 30%, 35% and 35% of the cortical thickness, respectively⁷⁸. In the pattern correlation analysis in Fig. 3, we used 3dVol2Surf in AFNI for projecting volume data onto the surface,

which employed an equidistance algorithm. According to our previous study⁴², equivolume and equidistance estimates of cortical depth showed only mild differences.

In bSSFP analysis, to generate the continuous laminar profiles shown in Fig. 2j, the relative cortical depth from 0 to 1 was resampled into 31 points, and the mean response at each depth was computed by averaging the grey matter voxels near that depth with Gaussian weights ($\sigma = 0.1$). Voxels in the cerebrospinal fluid or WM were not included. Pial and WM boundaries were manually delineated on the basis of the anatomical contrast of bSSFP and GRE images.

ROI definition. In Exp. 1, V1 ROIs were manually drawn on the cortical surface to select regions with a clear and balanced pattern of ODCs (see Extended Data Fig. 3a for the OD patterns and ROIs of all participants). Vertices with significant ocular bias (LE–RE abs(t) $>$ 2) and visual response (LE + RE $t >$ 2) were then projected into the volume space to select voxels in a column-wise manner. IPS ROIs were defined as the union of IPS0 to IPS5 in the Wang15 atlas⁴⁶, generated using the neuroptathy package (v0.12.13). The posterior and anterior IPS were defined as IPS0-2 and IPS3-5, respectively.

In Exp. 2, an anatomical mask for each LGN was manually delineated in the anatomical images. Two clusters of voxels with significant ocular bias (LE–RE abs(t) $>$ 2; for a few LGNs, the threshold was relaxed to 1.5 or 1) were identified for each LGN (see Extended Data Fig. 8 for all participants). V1 voxels with significant ocular bias (LE–RE abs(t) $>$ 2) and positive visual response (LE + RE $>$ 0) were included for ROI analysis. The pulvinar mask was manually delineated in the T1w MNI template, transformed to each participant's native space and then manually edited to ensure clear separation from the LGN. Finally, visually responsive voxels (LE + RE $t >$ 1) in the localizer were included as the ROI for the multivariate analysis.

Eye-specific response time course time-locked to the perceptual transition. Event-related eye-specific responses—that is, the difference in BOLD activity when participants perceived the stimulus from one eye over the other, time-locked to button presses—were estimated using several methods that generally led to similar results. To reduce the impact of HRF difference among brain areas (especially for subcortical nuclei), a model-free event-related average approach was used in most cases (Figs. 2b,c,e, 4c, 5c and so on). BOLD signals were averaged within each ROI (for the IPS, multivariate differential response was used), linearly interpolated ($dt = 0.1$ s) and segmented into epochs aligned to button presses. Trials $<$ 4 s or preceded by trials $<$ 2 s were excluded, as were unmatched button presses across rivalry and replay runs. Epochs were baseline corrected (-1 to 1 s mean; omitted for decoding time courses for which zero is a natural baseline) and averaged. The modulation time course was obtained by subtracting responses to the LE and RE events. For univariate differential signals, the results from LE- and RE-biased voxels were averaged (sign-flip for RE). Modulation amplitude was defined as the mean response 4–12 s post-switch. The response map of rivalry modulation was similarly calculated but by first projecting the BOLD time series onto the surface. The resulting map was high-pass filtered by subtracting its smoothed version (8-mm full width at half maximum (FWHM) surface smoothing; Fig. 2c).

To discount the influence of sluggish BOLD signal from previous trials, we estimated the modulation amplitude in V1 laminar analysis using a GLM (AFNI 3dDeconvolve, CSPLINzero model with nine spline parameters, 0–24 s post-switch, endpoints fixed at zero), which had a high SNR in V1 (Fig. 2f and Extended Data Fig. 5). Voxels for each eye and layer were averaged before being fed to the model. LE and RE events were modelled separately, and their results were differentiated (preferred minus non-preferred) and then averaged between LE and RE ODCs to get the modulation curve (Extended Data Fig. 5a). The amplitude was the mean under the first positive peak.

Non-eye-specific response time course time-locked to the perceptual transition. To measure transition-related responses to perceptual switches (Fig. 4f and Extended Data Fig. 7c), BOLD activity was detrended, averaged across LE- and RE-biased voxels and each condition (rivalry and replay), and then averaged across LE- and RE-dominant events. To avoid the influence of HRF difference across brain regions, we calculated the response delay of the transition-related response in rivalry relative to replay for each ROI and then compared the relative delays between ROIs. Transition-related responses were first averaged across participants, and the relative delay between rivalry and replay responses was estimated using the cross-correlation method (that is, to find the lag that gives the largest correlation). The 95% CIs and the *P* values were derived by bootstrapping participants.

Pattern correlation analysis. To quantify the synchronization of rivalry dynamics across ODCs in V1 (Fig. 3), we computed Pearson's correlation coefficient between the moment-to-moment V1 response pattern during rivalry and replay with the ODC pattern from the localizer. Pattern correlation was performed on the cortical surface. The volume-to-surface projection used the median map-function. Pattern correlation is less sensitive to difference in modulation amplitude, as larger modulation tend to show larger spatial standard deviation, which is normalized in the denominator of correlation coefficient. If one eye's ODCs become activated at slightly different times, or their modulation amplitudes vary asynchronously across the visual field, the correlation coefficient would be closer to zero on average. Thus, the width of the distribution of all *r* values in the TR-by-TR pattern correlation time course can be used as an index for the synchrony of eye-specific dynamics. The distribution width was defined as twice the standard deviation, estimated separately for each layer and condition. Since SNR, which may vary across layers, also limits the maximally attainable pattern correlation, we used the distribution width in the replay condition (where the response was synchronized by external stimulus drive) as a benchmark to measure the synchrony of rivalry dynamics.

In a control analysis, we tested whether the SNR difference across cortical layers alone could produce a similar laminar profile of pattern correlation. We first modelled the BOLD responses in the rivalry and replay conditions and within each layer using GLMs. LE- and RE-dominant intervals were modelled as two separate regressors with variable-length blocks (dmUBLOCK in AFNI). The residuals of the GLMs were shuffled across TRs, independently for each vertex, which destroyed any unmodelled synchronous activity fluctuation (for example, trial-by-trial changes in response amplitude that were synchronous across ODCs). The shuffled residuals were then added back to the fitted time series, and the same pattern correlation analysis was repeated for this generated dataset (Extended Data Fig. 6i).

This control analysis defined a null hypothesis that the distribution width of the moment-to-moment pattern correlation does not depend on the temporally synchronized structure across space in the GLM residuals, so that we are free to shuffle the residuals across time independently for each voxel, without impacting the *r*-distribution width ratio. To conduct a formal permutation test against this null hypothesis, the procedure was repeated 200 times to construct a null distribution for the statistic of interest (laminar difference in *r*-distribution width ratio), and the *P* value was derived on the basis of the percentile of the observed value in the null distribution (Extended Data Fig. 6j).

Multivariate SVM analysis of eye-specific response. To calculate the multivariate eye-specific response (Fig. 4 and Extended Data Fig. 7), a linear SVM classifier was trained by the localizer data to predict which eye was stimulated on a TR-by-TR basis (using the scikit-learn package (v0.24.2) with the default hyper-parameters). For each TR in rivalry and replay, the multivariate response patterns can then be linearly projected using the SVM weights that reflect the distance to the decision boundary. This decoding time series is the multivariate differential response.

Feature selection was used in SVM decoding. Within the anatomical mask of the ROI, voxels with above-threshold visual response (omni-bus $F > 1$, $L + R t > 1$, $L + R \beta < 5$) and ocular bias (200 most biased voxels ($2 \times$ up-sampled) in both ends of the L-R *t* distribution, with positive monocular response—for example, $LE > 0$ for LE-biased voxels) in the localizer were selected as features. The results were similar across a reasonable range of thresholds. The ideal response time course for the localizer was created by convolving the HRF (GAM with the default parameters in AFNI) with boxcar functions indicating LE or RE blocks and then taking their difference. Volumes at the flat part of the block responses (absolute value of the ideal response $> 0.75 \times$ maximum) were selected for training, whereas all volumes from the rivalry/replay runs were used at test time for generating the multivariate differential response. Each sample (feature vector) was normalized to have unitary Euclidean norm before training or testing.

DCM. The effective connectivity of the fMRI data was analysed with the DCM module of SPM12 (v.7771; Fig. 4e and Extended Data Fig. 7b). Multivariate decoding time series from V1, V2 and the IPS were used as VOI inputs. The time series of the rivalry and replay conditions were concatenated and modelled together. The model (Fig. 4e inset) included two inputs: the eye-of-origin of the currently perceived stimulus (high for LE and low for RE) was defined as a driving input to V1 in the replay condition, while all brain areas (V1/V2/IPS) could receive such an eye-specific driving input during rivalry. Fixed connections were defined between and within all brain areas, and the inter-area connections were allowed to be modulated by the second input during binocular rivalry. Both inputs were mean-centred. A bilinear, single-state, deterministic model with the default parameters was used. At the first or individual level, the full DCM for each participant was estimated using all data from the rivalry and replay runs. At the second or group level, we used the parametric empirical Bayes method to perform Bayesian model reduction and Bayesian model average and make inferences about the connectivity strength. The default parameters and priors were used during model fitting. Both the C matrix for the second input and the B matrix of the modulatory effect of rivalry were tested, and the averaged model for explaining the commonalities across participants was shown. *Z* values for the estimated parameters (for example, changes in effective connectivity—that is, the B matrix) were computed by dividing their expectation (Ep) by the square root of the corresponding diagonal elements in the covariance matrix (Cp).

Statistical analysis. Statistical analyses were conducted using the Pingouin package (v.0.5), JASP (v.0.14) and home-built Python code (for permutation and bootstrap procedures). A cluster-based permutation test⁷⁹ was employed to test the difference in time series correcting for multiple comparisons. Perceptual modulations were tested against zero using one-tailed one-sample *t*-tests and Holm correction for multiple comparisons across ROIs and conditions (unless otherwise noted). Differences in condition means were tested using repeated-measures analysis of variance (ANOVA) followed by two-tailed paired *t*-tests with Holm correction across ROIs (unless otherwise noted). The pairwise comparisons between different layers followed by a significant ANOVA were not corrected, as there were only three levels. Negative comparison results between group means were assessed using Bayes factor analysis (reporting BF_{01}) in Pingouin, employing the default JZS prior (Cauchy scale factor $r = 0.707$) as commonly recommended for *t*-tests. This approach allows for the evaluation of evidence in favour of the null hypothesis ($\delta = 0$) versus the alternative hypothesis ($\delta - \text{Cauchy}(0, 0.707)$) by comparing their marginal likelihoods, but does not focus on providing a posterior for the parameters. A range of other values ($r = 0.5$ and 1) was tested to ensure that the choice of prior did not qualitatively change the result. When comparing eye-specific modulation in rivalry and replay across ROIs, data for each ROI were normalized by dividing the L2-norm of all

participants' responses in both conditions (Fig. 4d). The normalization removed the difference in absolute response level in different ROIs but would not change the test results against zero or between rivalry and replay conditions, as the modulation of each participant in each condition was divided by the same value for a given ROI.

To account for the correlation between vertices or voxels in assessing the between-session consistency of OD patterns in V1 and LGN, the observed correlation coefficients were compared with the null distribution via Monte Carlo simulation. The spatial autocorrelation function within the ROI was first estimated from the localizer GLM residual volumes (3dFWHMx in AFNI using the three-parameter ACF model). Then, 10,000 simulated volumes (Gaussian random noise with specified spatial smoothness) were generated (3dClustSim in AFNI) as surrogate data, with which correlation coefficients under the null hypothesis were computed to get the null distribution. Finally, the observed statistic was compared to the critical value of the null distribution for its significance.

Reporting summary

Further information on research design is available in the Nature Portfolio Reporting Summary linked to this article.

Data availability

Data to reproduce the main findings of this study can be downloaded from the National Basic Science Data Center at <https://www.scidb.cn/en/s/ZJVBza>. The raw data can be requested by contacting the corresponding author. Source data are provided with this paper.

Code availability

The mripy package, used in this study for high-resolution fMRI data processing, is available via GitHub at <https://github.com/herrlich10/mripy>.

References

1. Blake, R. & Logothetis, N. K. Visual competition. *Nat. Rev. Neurosci.* **3**, 13–23 (2002).
2. Blake, R., Brascamp, J. & Heeger, D. J. Can binocular rivalry reveal neural correlates of consciousness? *Philos. Trans. R. Soc. Lond. B* **369**, 20130211 (2014).
3. Crick, F. Visual perception: rivalry and consciousness. *Nature* **379**, 485–486 (1996).
4. Tong, F., Meng, M. & Blake, R. Neural bases of binocular rivalry. *Trends Cogn. Sci.* **10**, 502–511 (2006).
5. Blake, R. A neural theory of binocular rivalry. *Psychol. Rev.* **96**, 145–167 (1989).
6. Dougherty, K., Schmid, M. C. & Maier, A. Binocular response modulation in the lateral geniculate nucleus. *J. Comp. Neurol.* **527**, 522–534 (2018).
7. Guillory, R. W. & Colonnier, M. Synaptic patterns in the dorsal lateral geniculate nucleus of the monkey. *Z. Zellforsch. Mikrosk. Anat.* **103**, 90–108 (1970).
8. Markram, H. et al. Interneurons of the neocortical inhibitory system. *Nat. Rev. Neurosci.* **5**, 793–807 (2004).
9. Tong, F. & Engel, S. A. Interocular rivalry revealed in the human cortical blind-spot representation. *Nature* **411**, 195–199 (2001).
10. Haynes, J. D., Deichmann, R. & Rees, G. Eye-specific effects of binocular rivalry in the human lateral geniculate nucleus. *Nature* **438**, 496–499 (2005).
11. Lehky, S. R. & Maunsell, J. H. R. No binocular rivalry in the LGN of alert macaque monkeys. *Vis. Res.* **36**, 1225–1234 (1996).
12. Leopold, D. A. & Logothetis, N. K. Activity changes in early visual cortex reflect monkeys' percepts during binocular rivalry. *Nature* **379**, 549–553 (1996).
13. Maier, A. et al. Divergence of fMRI and neural signals in V1 during perceptual suppression in the awake monkey. *Nat. Neurosci.* **11**, 1193–1200 (2008).
14. Logothetis, N. K. & Wandell, B. A. Interpreting the BOLD signal. *Annu. Rev. Physiol.* **66**, 735–769 (2004).
15. Zhang, P., Jiang, Y. & He, S. Voluntary attention modulates processing of eye-specific visual information. *Psychol. Sci.* **23**, 254–260 (2012).
16. Maunsell, J. H. R. & Van Essen, D. C. Functional properties of neurons in middle temporal visual area of the macaque monkey. II. Binocular interactions and sensitivity to binocular disparity. *J. Neurophysiol.* **49**, 1148–1167 (1983).
17. Zaretskaya, N. et al. Eye-selective fMRI activity in human primary visual cortex: comparison between 3 T and 9.4 T, and effects across cortical depth. *NeuroImage* **220**, 117078 (2020).
18. Logothetis, N. K., Leopold, D. A. & Sheinberg, D. L. What is rivalry during binocular rivalry? *Nature* **380**, 621–624 (1996).
19. Hesse, J. K. & Tsao, D. Y. A new no-report paradigm reveals that face cells encode both consciously perceived and suppressed stimuli. *eLife* **9**, e58360 (2020).
20. Tong, F., Nakayama, K., Vaughan, J. T. & Kanwisher, N. Binocular rivalry and visual awareness in human extrastriate cortex. *Neuron* **21**, 753–759 (1998).
21. Brascamp, J., Sterzer, P., Blake, R. & Knapen, T. Multistable perception and the role of the frontoparietal cortex in perceptual inference. *Annu. Rev. Psychol.* **69**, 77–103 (2018).
22. Lumer, E. D., Friston, K. J. & Rees, G. Neural correlates of perceptual rivalry in the human brain. *Science* **280**, 1930–1934 (1998).
23. Knapen, T., Brascamp, J., Pearson, J., van Ee, R. & Blake, R. The role of frontal and parietal brain areas in bistable perception. *J. Neurosci.* **31**, 10293–10301 (2011).
24. Frasle, S. et al. Binocular rivalry: frontal activity relates to introspection and action but not to perception. *J. Neurosci.* **34**, 1738–1747 (2014).
25. Brascamp, J., Blake, R. & Knapen, T. Negligible fronto-parietal BOLD activity accompanying unreportable switches in bistable perception. *Nat. Neurosci.* **18**, 1672–1678 (2015).
26. Zou, J., He, S. & Zhang, P. Binocular rivalry from invisible patterns. *Proc. Natl Acad. Sci. USA* **113**, 8408–8413 (2016).
27. Brascamp, J. W. & Blake, R. Inattention abolishes binocular rivalry: perceptual evidence. *Psychol. Sci.* **23**, 1159–1167 (2012).
28. Zhang, P., Jamison, K., Engel, S., He, B. & He, S. Binocular rivalry requires visual attention. *Neuron* **71**, 362–369 (2011).
29. Kapoor, V. et al. Decoding internally generated transitions of conscious contents in the prefrontal cortex without subjective reports. *Nat. Commun.* **13**, 1535 (2022).
30. Dwarakanath, A. et al. Bistability of prefrontal states gates access to consciousness. *Neuron* **111**, 1666–1683.e4 (2023).
31. Kovács, I., Papathomas, T. V., Yang, M. & Fehér, A. When the brain changes its mind: interocular grouping during binocular rivalry. *Proc. Natl Acad. Sci. USA* **93**, 15508–15511 (1996).
32. Kim, S. G. & Fukuda, M. Lessons from fMRI about mapping cortical columns. *Neuroscientist* **14**, 287–299 (2008).
33. Van de Moortele, P. F. et al. T1 weighted brain images at 7 Tesla unbiased for proton density, T2* contrast and RF coil receive B1 sensitivity with simultaneous vessel visualization. *NeuroImage* **46**, 432–446 (2009).
34. Scheffler, K., Heule, R., Báez-Yáñez, M. G., Kardatzki, B. & Lohmann, G. The BOLD sensitivity of rapid steady-state sequences. *Magn. Reson. Med.* **81**, 2526–2535 (2019).
35. Cheng, K., Waggoner, R. A. & Tanaka, K. Human ocular dominance columns as revealed by high-field functional magnetic resonance imaging. *Neuron* **32**, 359–374 (2001).
36. Yacoub, E., Shmuel, A., Logothetis, N. & Ugurbil, K. Robust detection of ocular dominance columns in humans using Hahn Spin Echo BOLD functional MRI at 7 Tesla. *NeuroImage* **37**, 1161–1177 (2007).

37. de Hollander, G., van der Zwaag, W., Qian, C., Zhang, P. & Knapen, T. Ultra-high field fMRI reveals origins of feedforward and feedback activity within laminae of human ocular dominance columns. *NeuroImage* **228**, 117683 (2021).
38. Adams, D. L., Sincich, L. C. & Horton, J. C. Complete pattern of ocular dominance columns in human primary visual cortex. *J. Neurosci.* **27**, 10391–10403 (2007).
39. Moon, C. H., Fukuda, M., Park, S. H. & Kim, S. G. Neural interpretation of blood oxygenation level-dependent fMRI maps at submillimeter columnar resolution. *J. Neurosci.* **27**, 6892–6902 (2007).
40. Waehnert, M. D. et al. Anatomically motivated modeling of cortical laminae. *NeuroImage* **93**, 210–220 (2014).
41. Uludag, K. & Havlicek, M. Determining laminar neuronal activity from BOLD fMRI using a generative model. *Prog. Neurobiol.* **207**, 102055 (2021).
42. Liu, C. et al. Layer-dependent multiplicative effects of spatial attention on contrast responses in human early visual cortex. *Prog. Neurobiol.* **207**, 101897 (2021).
43. O’Hashi, K. et al. Interhemispheric synchrony of spontaneous cortical states at the cortical column level. *Cereb. Cortex* **28**, 1794–1807 (2018).
44. Zaretskaya, N., Thielscher, A., Logothetis, N. K. & Bartels, A. Disrupting parietal function prolongs dominance durations in binocular rivalry. *Curr. Biol.* **20**, 2106–2111 (2010).
45. Zaretskaya, N. & Narinyan, M. Introspection, attention or awareness? The role of the frontal lobe in binocular rivalry. *Front. Hum. Neurosci.* **8**, 527 (2014).
46. Wang, L., Mruczek, R. E. B., Arcaro, M. J. & Kastner, S. Probabilistic maps of visual topography in human cortex. *Cereb. Cortex* **25**, 3911–3931 (2015).
47. Qian, Y. et al. Robust functional mapping of layer-selective responses in human lateral geniculate nucleus with high-resolution 7T fMRI. *Proc. R. Soc. B* **287**, 20200245 (2020).
48. Tootell, R. B. H. et al. The retinotopy of visual spatial attention. *Neuron* **21**, 1409–1422 (1998).
49. Shmuel, A. et al. Sustained negative BOLD, blood flow and oxygen consumption response and its coupling to the positive response in the human brain. *Neuron* **36**, 1195–1210 (2002).
50. Wunderlich, K., Schneider, K. A. & Kastner, S. Neural correlates of binocular rivalry in the human lateral geniculate nucleus. *Nat. Neurosci.* **8**, 1595–1602 (2005).
51. Felleman, D. J. & Van Essen, D. C. Distributed hierarchical processing in the primate cerebral cortex. *Cereb. Cortex* **1**, 1–47 (1991).
52. Tremblay, R., Lee, S. & Rudy, B. GABAergic interneurons in the neocortex: from cellular properties to circuits. *Neuron* **91**, 260–292 (2016).
53. Kisvárdy, Z. F. Chapter 18 GABAergic networks of basket cells in the visual cortex. *Prog. Brain Res.* **90**, 385–405 (1992).
54. Kisvárdy, Z. F., Beaulieu, C. & Eysel, U. T. Network of GABAergic large basket cells in cat visual cortex (area 18): implication for lateral disinhibition. *J. Comp. Neurol.* **327**, 398–415 (1993).
55. Wang, Y. et al. Anatomical, physiological and molecular properties of Martinotti cells in the somatosensory cortex of the juvenile rat. *J. Physiol.* **561**, 65–90 (2004).
56. Buzs, P., Eysel, U. T., Adorján, P. & Kisvárdy, Z. F. Axonal topography of cortical basket cells in relation to orientation, direction, and ocular dominance maps. *J. Comp. Neurol.* **437**, 259–285 (2001).
57. Gilbert, C. D. & Wiesel, T. N. Clustered intrinsic connections in cat visual cortex. *J. Neurosci.* **3**, 1116–1133 (1983).
58. Rockland, K. S. & Lund, J. S. Intrinsic laminar lattice connections in primate visual cortex. *J. Comp. Neurol.* **216**, 303–318 (1983).
59. Angelucci, A. et al. Circuits and mechanisms for surround modulation in visual cortex. *Annu. Rev. Neurosci.* **40**, 425–451 (2017).
60. Adesnik, H. & Scanziani, M. Lateral competition for cortical space by layer-specific horizontal circuits. *Nature* **464**, 1155–1160 (2010).
61. Cox, M. A., Dougherty, K., Westerberg, J. A., Schall, M. S. & Maier, A. Temporal dynamics of binocular integration in primary visual cortex. *J. Vis.* **19**, 13 (2019).
62. Sengpiel, F., Blakemore, C. & Harrad, R. Interocular suppression in the primary visual cortex: a possible neural basis of binocular rivalry. *Vis. Res.* **35**, 179–195 (1995).
63. Shipp, S. The functional logic of cortico-pulvinar connections. *Philos. Trans. R. Soc. Lond. B* **358**, 1605–1624 (2003).
64. Meyer, H. S. et al. Inhibitory interneurons in a cortical column form hot zones of inhibition in layers 2 and 5A. *Proc. Natl Acad. Sci. USA* **108**, 16807–16812 (2011).
65. Buzsáki, G., Kaila, K. & Raichle, M. Inhibition and brain work. *Neuron* **56**, 771–783 (2007).
66. Moon, H. S. et al. Contribution of excitatory and inhibitory neuronal activity to BOLD fMRI. *Cereb. Cortex* **31**, 4053–4067 (2021).
67. Schroeder, C. E., Tenke, C. E., Arezzo, J. C. & Vaughan, H. G. Binocularity in the lateral geniculate-nucleus of the alert macaque. *Brain Res.* **521**, 303–310 (1990).
68. Dougherty, K., et al. Binocular suppression in the macaque lateral geniculate nucleus reveals early competitive interactions between the eyes. *eNeuro* **8**, ENEURO.0364-20.2020 (2021).
69. Yıldırım, I. & Schneider, K. A. Neural dynamics during binocular rivalry: indications from human lateral geniculate nucleus. *eNeuro* **10**, ENEURO.0470-22.2022 (2023).
70. O’Connor, D. H., Fukui, M. M., Pinsk, M. A. & Kastner, S. Attention modulates responses in the human lateral geniculate nucleus. *Nat. Neurosci.* **5**, 1203–1209 (2002).
71. Rafal, R., Henik, A. & Smith, J. Extrageniculate contributions to reflex visual orienting in normal humans: a temporal hemifield advantage. *J. Cogn. Neurosci.* **3**, 322–328 (1991).
72. de Jong, M. C. et al. Intracranial recordings reveal unique shape and timing of responses in human visual cortex during illusory visual events. *Curr. Biol.* **30**, 3089–3100.e4 (2020).
73. Xu, H. et al. Rivalry-like neural activity in primary visual cortex in anesthetized monkeys. *J. Neurosci.* **36**, 3231–3242 (2016).
74. Pearson, J. New directions in mental-imagery research: the binocular-rivalry technique and decoding fMRI patterns. *Curr. Dir. Psychol. Sci.* **23**, 178–183 (2014).
75. Huber, L., Uludağ, K. & Möller, H. E. Non-BOLD contrast for laminar fMRI in humans: CBF, CBV, and CMRO₂. *NeuroImage* **197**, 742–760 (2019).
76. Ehses, P. & Scheffler, K. Multiline balanced SSFP for rapid functional imaging at ultrahigh field. *Magn. Reson. Med.* **79**, 994–1000 (2018).
77. Kay, K. et al. A critical assessment of data quality and venous effects in sub-millimeter fMRI. *NeuroImage* **189**, 847–869 (2019).
78. Balaram, P., Young, N. A. & Kaas, J. H. Histological features of layers and sublayers in cortical visual areas V1 and V2 of chimpanzees, macaque monkeys, and humans. *Eye Brain* **2014**, 5–18 (2014).
79. Nichols, T. E. & Holmes, A. P. Nonparametric permutation tests for functional neuroimaging: a primer with examples. *Hum. Brain Mapp.* **15**, 1–25 (2002).

Acknowledgements

This study was supported by STI2030-Major Projects (grant nos. 2021ZD0204200 to C.Q. and S.H. and 2022ZD0211900 to P.Z.), the National Natural Science Foundation of China (grant nos. 32000787 to C.Q. and 31871107 and 31930053 to P.Z.), the Chinese Academy

of Sciences (grant nos. KJZD-SW-L08 and YSBR-071 to S.H.), the Youth Innovation Promotion Association CAS (grant nos. 2021089 to C.Q. and 2022093 to Z.Z.), the National Key R&D Program of China (grant no. 2023YFF1203500 to C.Q.) and the CAS-NWO International Cooperation Program (grant nos. 153311KYSB20160030 to P.Z. and 012.200.012 to T.K.).

Author contributions

C.Q. and P.Z. conceived of and designed the experiments. C.Q., G.d.H., T.K. and P.Z. performed the experiments. Z.Z. provided technical support of MRI data acquisition. C.Q., Z.C., S.H. and P.Z. analysed the data. C.Q. and P.Z. contributed materials/analysis tools. C.Q., G.d.H., T.K., S.H. and P.Z. wrote the paper.

Competing interests

The authors declare no competing interests.

Additional information

Extended data is available for this paper at
<https://doi.org/10.1038/s41562-025-02320-4>.

Supplementary information The online version contains supplementary material available at
<https://doi.org/10.1038/s41562-025-02320-4>.

Correspondence and requests for materials should be addressed to Peng Zhang.

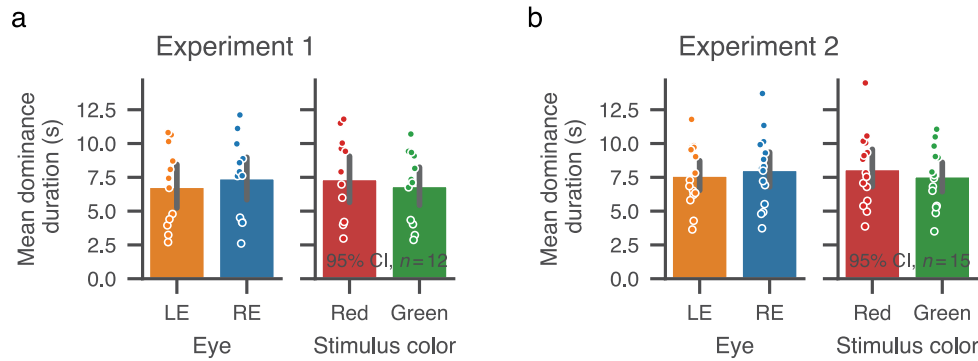
Peer review information *Nature Human Behaviour* thanks Keith Schneider and the other, anonymous, reviewer(s) for their contribution to the peer review of this work. Peer reviewer reports are available.

Reprints and permissions information is available at
www.nature.com/reprints.

Publisher's note Springer Nature remains neutral with regard to jurisdictional claims in published maps and institutional affiliations.

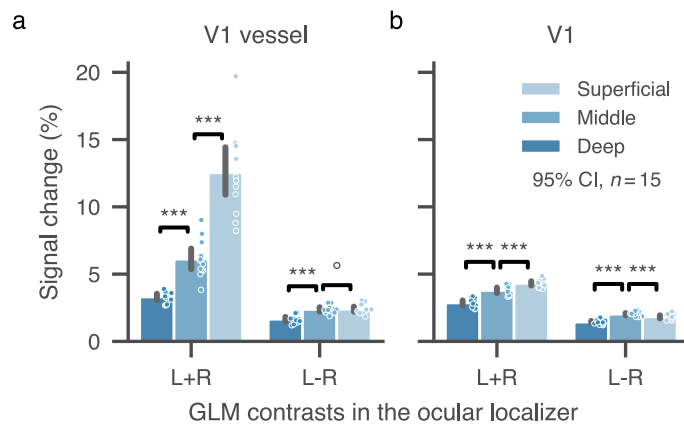
Open Access This article is licensed under a Creative Commons Attribution-NonCommercial-NoDerivatives 4.0 International License, which permits any non-commercial use, sharing, distribution and reproduction in any medium or format, as long as you give appropriate credit to the original author(s) and the source, provide a link to the Creative Commons licence, and indicate if you modified the licensed material. You do not have permission under this licence to share adapted material derived from this article or parts of it. The images or other third party material in this article are included in the article's Creative Commons licence, unless indicated otherwise in a credit line to the material. If material is not included in the article's Creative Commons licence and your intended use is not permitted by statutory regulation or exceeds the permitted use, you will need to obtain permission directly from the copyright holder. To view a copy of this licence, visit <http://creativecommons.org/licenses/by-nc-nd/4.0/>.

© The Author(s) 2025



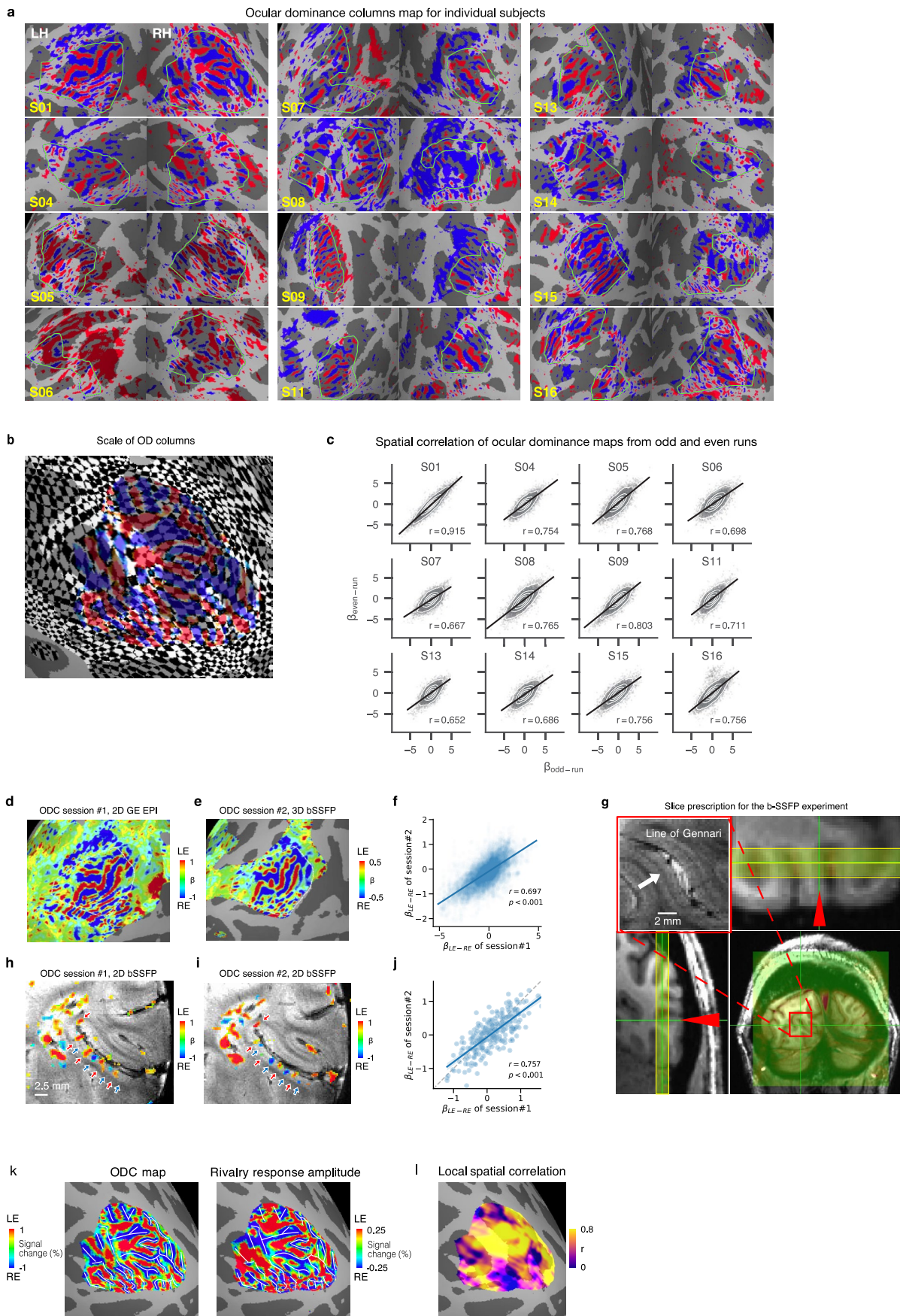
Extended Data Fig. 1 | Mean dominant durations for the two eyes and the two stimuli during binocular rivalry. (a) Mean duration in Exp.1. (b) Mean duration in Exp.2. The left panel of each figure shows the dominant durations for LE and RE percepts, and the right panel shows the dominant durations for the red and

green percepts. The association between eye and color (LE-red/RE-green, or vice versa) swapped every run in both experiments. Bar plots show mean values with 95% confidence intervals obtained by bootstrapping participants; individual data points are overlaid as dots.



Extended Data Fig. 2 | Laminar profiles of the overall visual response relative to baseline (LE + RE) and the eye-specific differential response (LE-RE) in localizer runs. (a) Laminar profiles of V1 columns contaminated by large vessels. (b) Laminar profiles for V1 voxels after vessel exclusion. Bar plots show mean values with 95% confidence intervals obtained by bootstrapping participants;

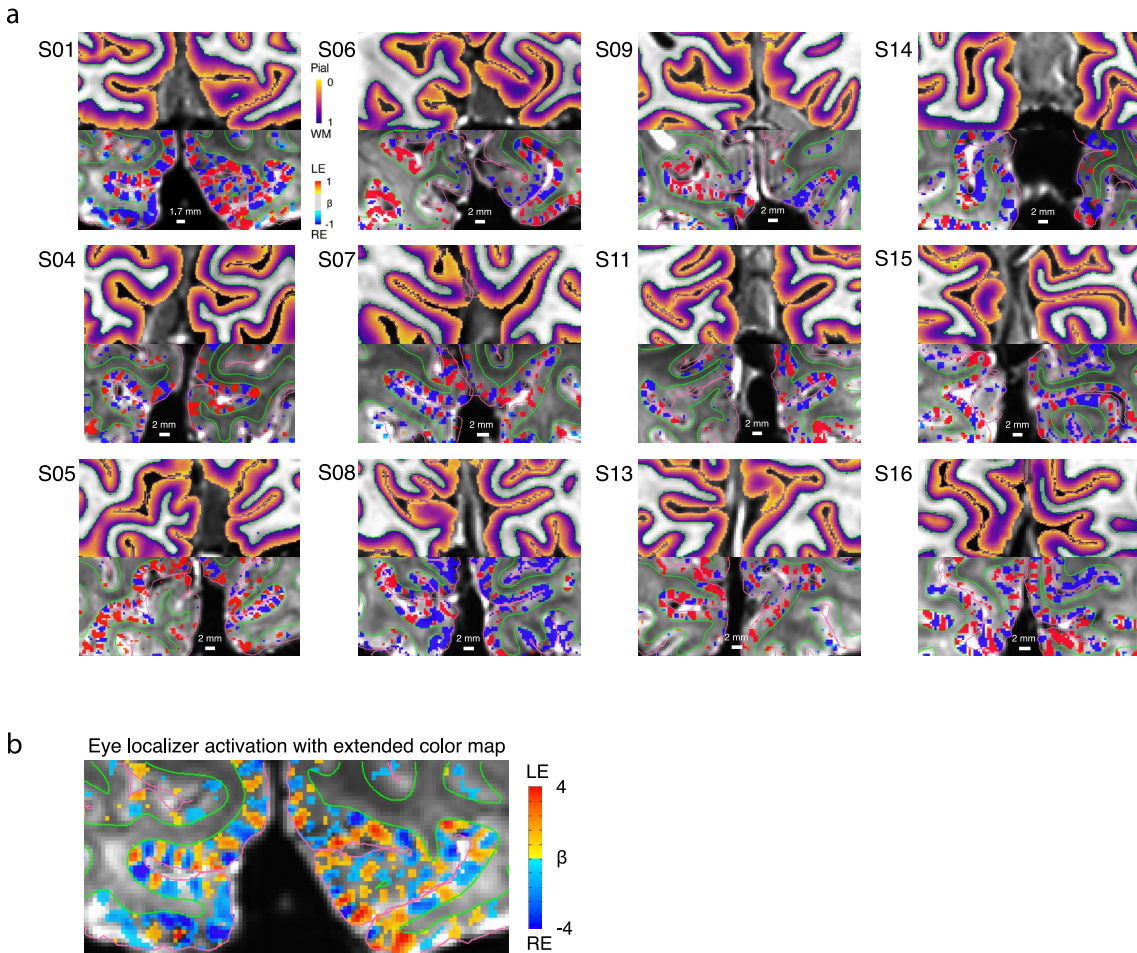
individual data points are overlaid as dots. Difference between layers was assessed by two-sided paired t-tests. Black asterisks: significant after Holm correction (**: $p < 0.001$); black circle: Bayes factor in favor of null hypothesis ($BF_01 > 3$; default JZS prior, Cauchy scale factor $r = 0.707$).



Extended Data Fig. 3 | See next page for caption.

Extended Data Fig. 3 | V1 ocular dominance column (ODC) patterns and reliability analyses. (a) ODC patterns for all participants in Exp. 1. Colors represent LE–RE percent signal change (two-sided t-statistics; $p < 0.05$ uncorrected). Green lines mark hand-drawn surface ROIs with roughly balanced ODCs. LH: left hemisphere; RH: right hemisphere (b) ODC widths on inflated cortical surface (S01). Black and white grids visualize the scale variation of 1 mm isotropic voxels projected to the surface. (c) Pattern correlations between ODC maps in odd and even runs for individual participants. Voxels in anatomically defined V1 showing significant visual responses (LE + RE $t > 2$, two-sided test uncorrected) in the first half of data were included. Beta values indicate LE–RE percent signal change. Each dot is one upsampled voxel. The black line shows the linear fit, and white contours reflect 2D kernel density. R values are Pearson's correlation. (d, e, f) ODC patterns (S01) acquired with GE-EPI and 3D bSSFP sequences in different days. Correlation

in (f) was computed within the white-outlined region. P-value was derived from a Monte Carlo test accounting for spatial dependence. (g) Slice prescriptions for the 2D-bSSFP experiment (S06, 0.5 mm in-plane, 3 mm thick, perpendicular to cortex). The line of Gennari is visible in the T2*-weighted GRE image (top left inset), confirming the perpendicular orientation. Views: axial (top right); sagittal: bottom left; coronal (bottom right). (h, i, j) ODC patterns from 2D bSSFP scans on two days (S06). Red/blue arrows mark LE/RE ODCs for comparison. Blue lines in (f/j) show linear fits. The gray dashed line in (j) marks the diagonal, omitted in (f) due to differing pulse sequences. (k) Comparison of ODC map (localizer) and eye-specific response pattern during rivalry (S01). White lines mark RE columns from the localizer, copied to the rivalry map for comparison. Color bars show percent signal change. (l) Local spatial correlation between the two maps in (k). Colors denote Pearson's correlation.

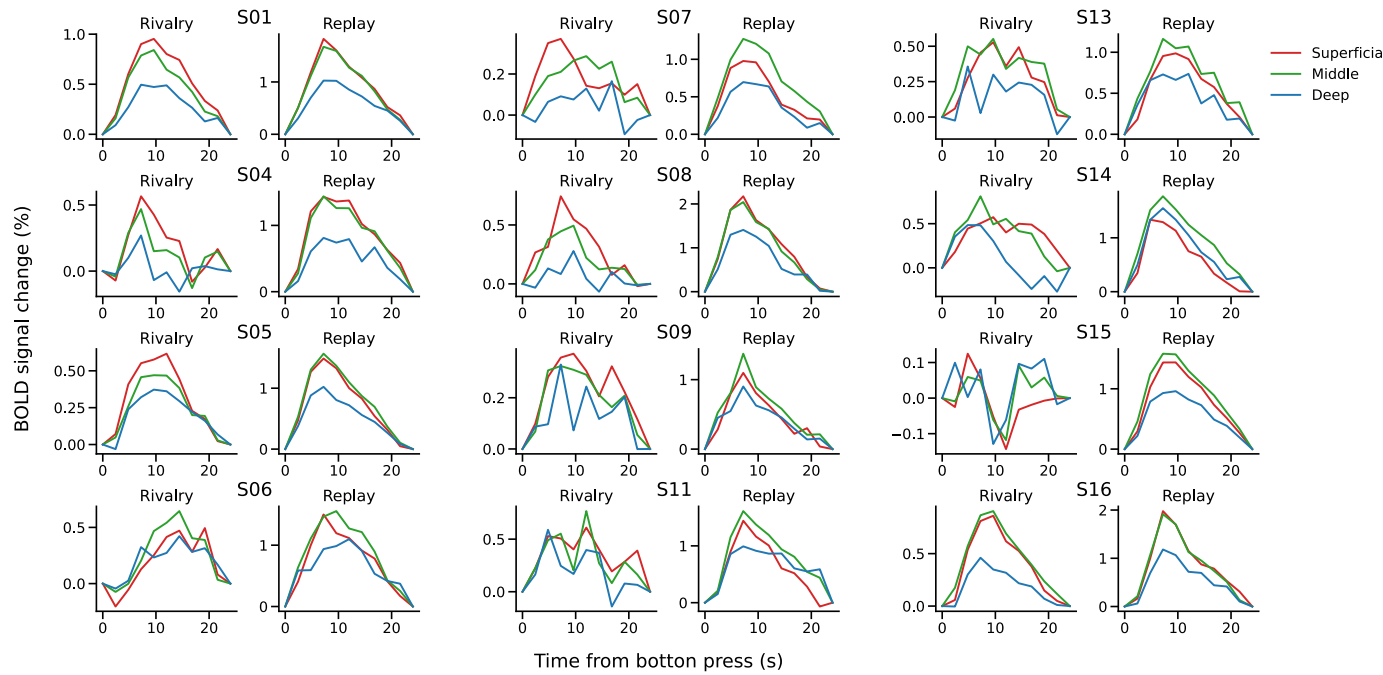


Extended Data Fig. 4 | Cortical segmentation and alignment for all participants in Exp. 1. **a**) Green and purple lines mark the white matter and pial surfaces. Top: relative cortical depth on a T1-weighted MP2RAGE; bottom: LE-RE percent signal

change ($p < 0.05$ uncorrected; two sided t-statistics) on mean EPI. Reds and blues indicate LE- and RE-biased voxels. Only activations in the gray matter were shown. **(b)**) Eye localizer activation (S01) with extended color map.

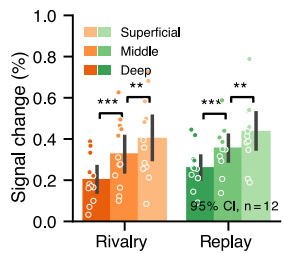
a

Eye-specific response for individual subjects

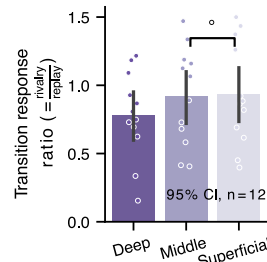


Transition-related response

b

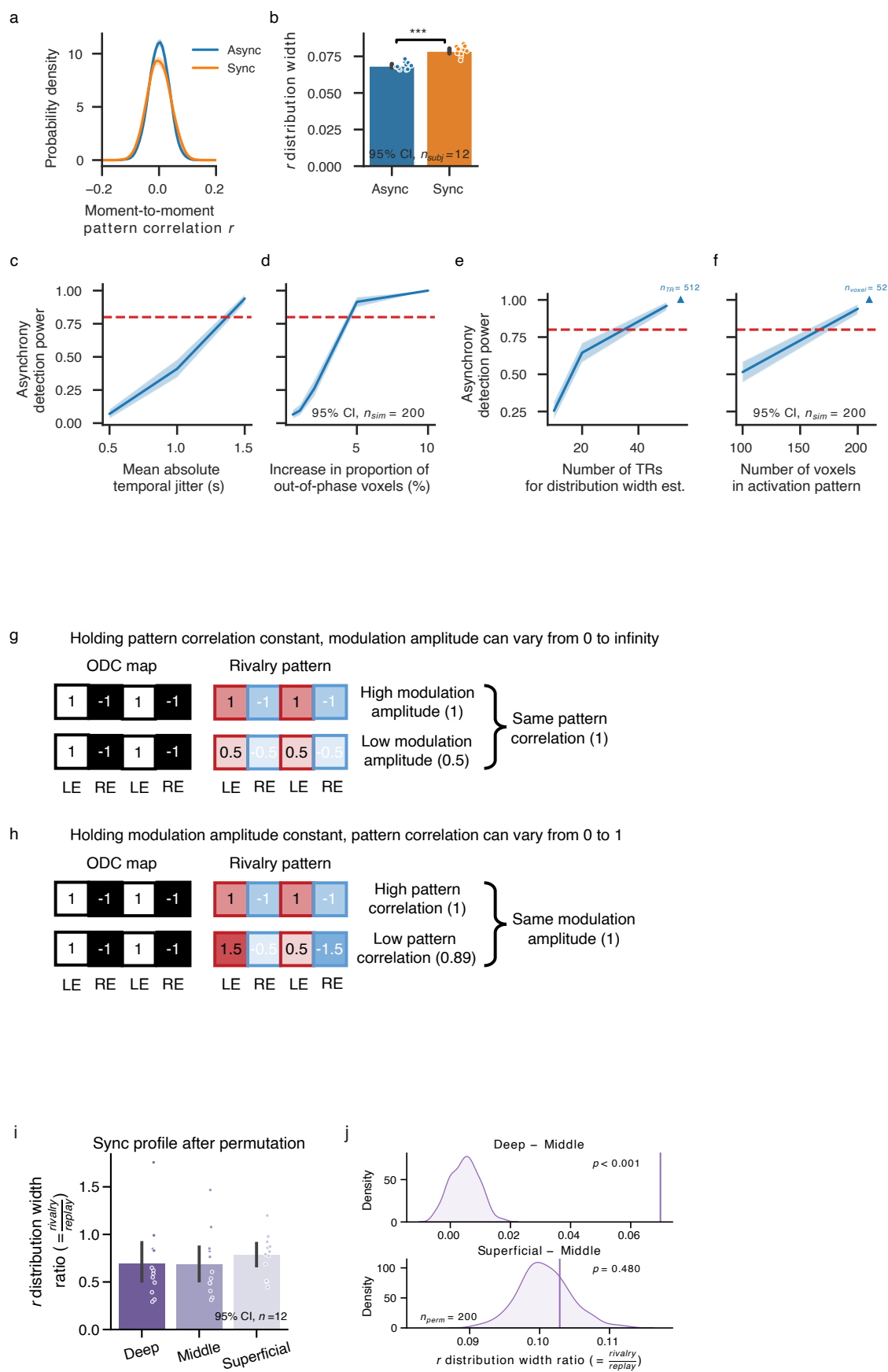


c



Extended Data Fig. 5 | Eye-specific and non-eye-specific responses in different V1 layers during rivalry and replay. (a) Eye-specific differential timecourses during rivalry and replay for all participants in Exp. 1, computed as the difference between the deconvolved responses to preferred- and non-preferred-eye events. Deconvolved responses were estimated using a GLM-based method (3dDeconvolve with CSPLINzero in AFNI) to account for BOLD carryover. Colors indicate cortical depth: red (superficial), green (middle), blue (deep). **(b)** Switch-related responses (the average of responses to LE- and RE-dominant events) across V1 layers. A significant superficial bias was found in both rivalry and replay conditions (repeated measures ANOVA main effect of layer, $F(2,22) = 40.123$,

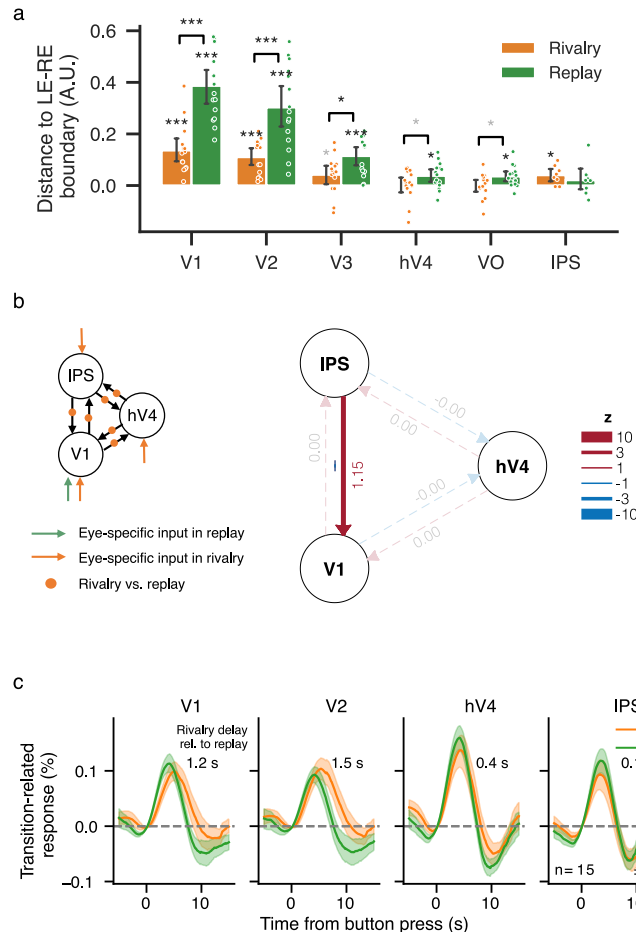
$p < 0.001$, $\eta^2 = 0.234$, 95% CI [0.137, 0.438]; no interaction between conditions and layers, $F(2,22) = 0.692$, $p = 0.483$, $\eta^2 = 0.002$, 95% CI [0.0, 0.027]). Two-sided paired t-tests for layer comparisons in b and cs: * $p < 0.05$, ** $p < 0.01$, *** $p < 0.001$, Holm corrected. **(c)** Rivalry/replay response ratio across cortical depths showed no significant differences (deep vs. middle, $t(11) = -2.238$, $p = 0.094$, Cohen's $d = 0.412$, 95% CI [-0.28, -0.0]; middle vs. superficial, $t(11) = -0.277$, $p = 0.787$, $d = 0.038$, 95% CI [-0.12, 0.1]; $BF_01 = 3.367$, marked by the black circle). Transition-related response amplitudes were estimated from the deconvolved timecourses using the same approach as in Fig. 2f for comparison.



Extended Data Fig. 6 | See next page for caption.

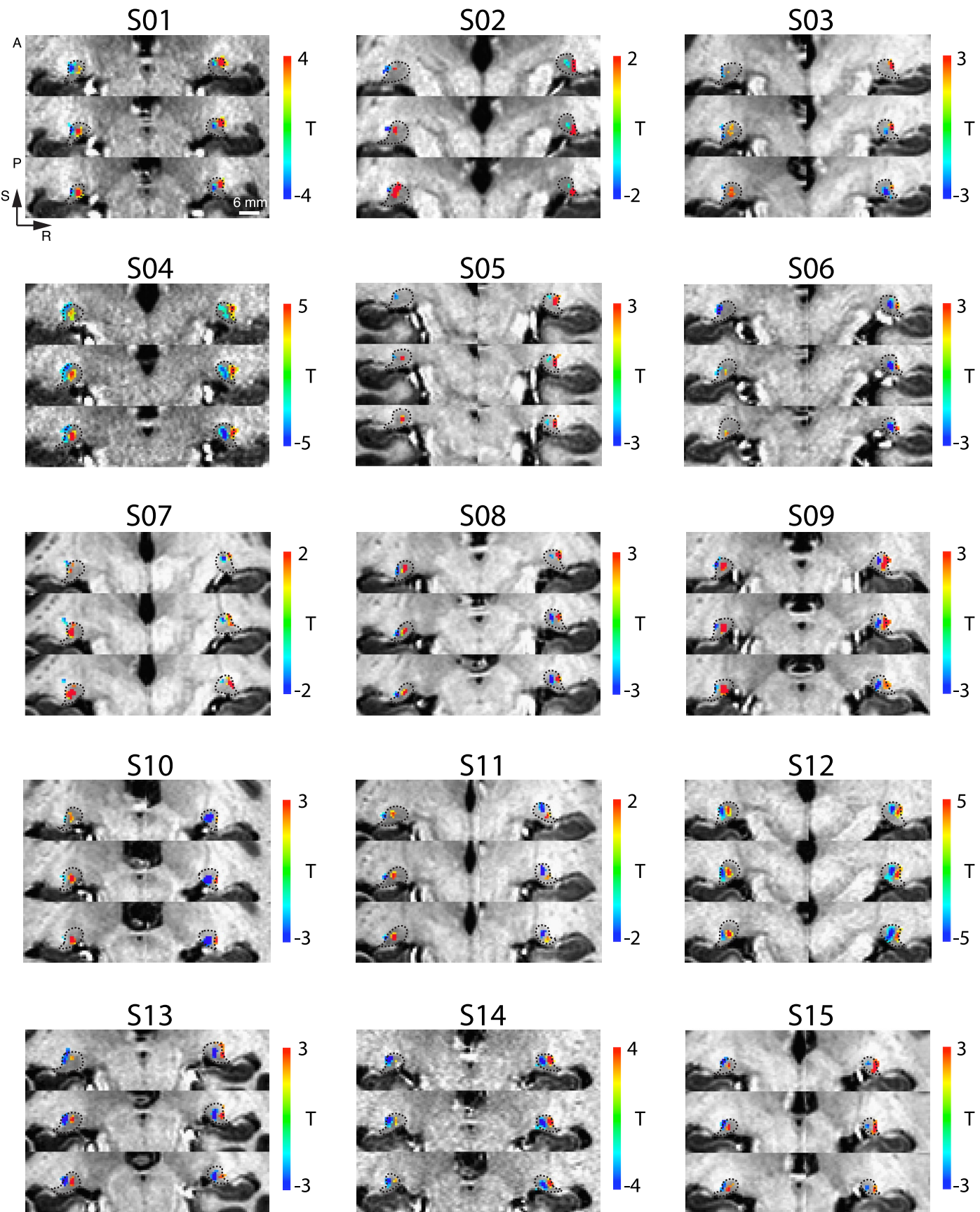
Extended Data Fig. 6 | Simulation and control analyses for pattern correlation during rivalry and replay. We ran simulations to demonstrate the ability of pattern correlation in capturing asynchrony across space and estimate the amount of asynchrony that can be reliably detected (supplementary methods). **(a)** Simulated distribution of pattern correlation coefficients for Async and Sync conditions. Async: 30% of voxels were out-of-phase, and voxel transitions had a 0–2 s jitter (mean 1 s); Sync: only 20% were out-of-phase and transitions were aligned. Line plot: mean \pm SEM across participants. **(b)** r distribution widths in the two conditions. Bar plot: mean with 95% CI across participants; dot plot: individual data; ***: $p < 0.001$, two-sided paired t-test. **(c)** Power analysis for pattern correlation to detect different levels of temporal jitter in voxel transition and **(d)** different proportions of out-of-phase voxels. **(e)** Minimum number of TRs and **(f)** voxels required to detect effects similar to (a). Shaded areas: 95% CI (bootstrap); red dashed line: 80% power. Blue triangles mark actual values in Exp. 1. **(g–h)** Conceptual dissociation between pattern correlation and mean modulation amplitude. A schematic illustrates a cortical patch with alternating

LE- and RE-dominant columns (white/black). Pattern correlation is computed using a binary template (1, -1), while modulation amplitude averages across all columns. **(g)** Two patterns with equal correlation ($r = 1$) differ in modulation amplitude (1 vs. 0.5). **(h)** Two patterns with identical modulation amplitude (1) show different correlations with the template ($r = 1$ vs. 0.89). This illustrates the complementary nature of pattern correlation and mean modulation amplitude in characterizing cortical activation during rivalry. **(i–j)** Permutation analysis controlling for SNR-related confound in laminar pattern correlation. **(i)** After temporally shuffling residuals to disrupt synchrony while preserving SNR, no significant laminar difference in the rivalry-to-replay ratio of r distribution width was observed ($F(2,22)=2.115$, $p = 0.165$, $ng_2 = 0.020$, 95% CI [0.002, 0.226]). Bayes factor analysis supported the null hypothesis that there was no difference between deep and middle layers ($BFO_1 = 3.257$, default JZS prior). **(j)** Null distributions of layer differences from 200 permutations (deep–middle, top; superficial–middle, bottom); observed differences in Exp. 1 are shown as vertical lines.

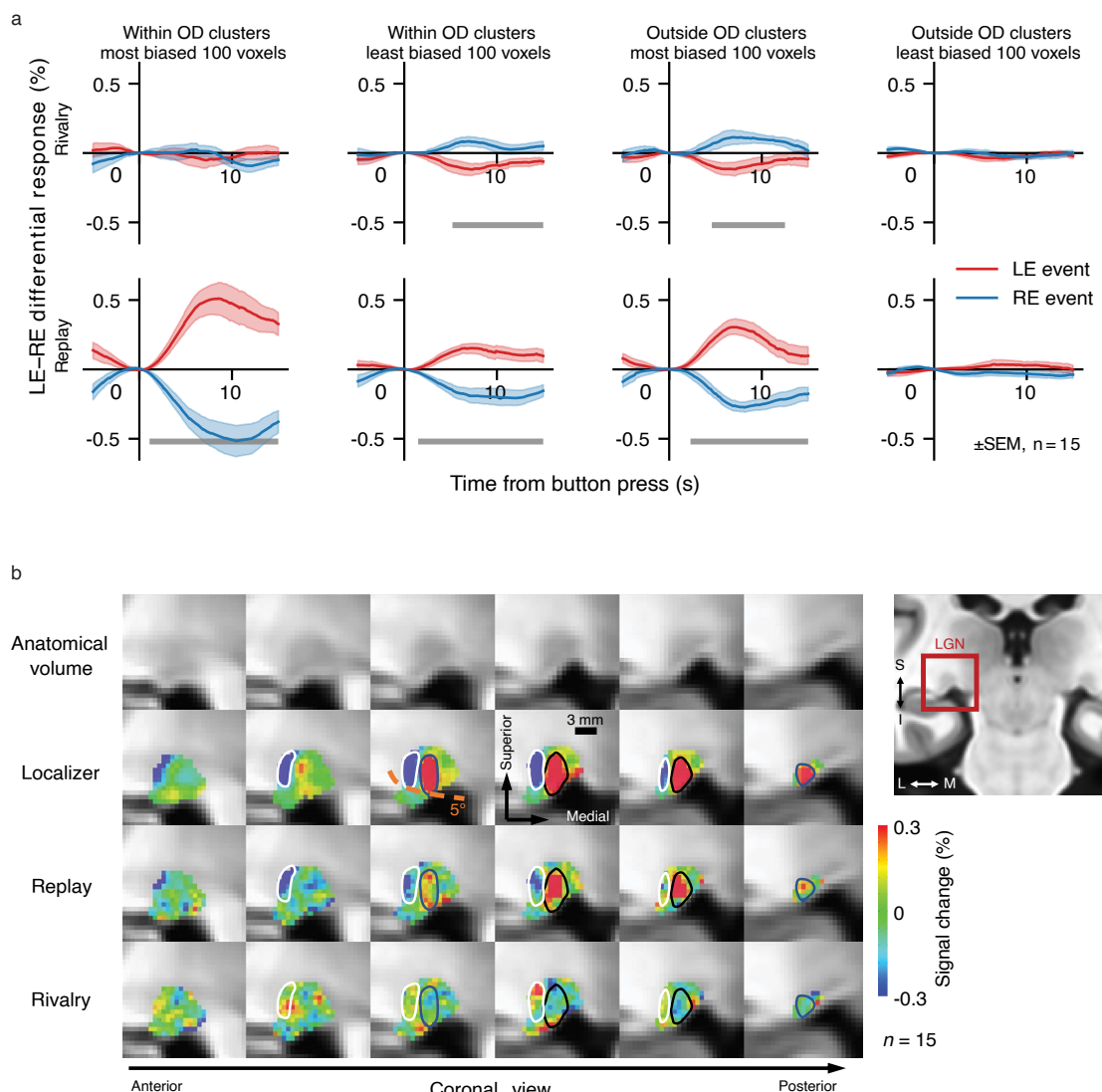


Extended Data Fig. 7 | Eye-specific modulation and perceptual switch dynamics across cortical areas during rivalry and replay (Exp. 2).
(a) Eye-specific modulation during rivalry (orange) and replay (green) in early (V1-V3), ventral (hV4/VO), and parietal (IPS) visual areas, quantified via multivariate methods. N=15 participants for all areas except IPS (n=8, due to limited coverage). Bar plot: mean values with 95% CI across participants; dot plot: individual data. Significance was tested against zero (one-tailed one-sample t-tests) and between conditions (two-tailed paired t-tests). Black stars: significant after Holm correction across ROIs and conditions; gray stars: uncorrected. * $p < 0.05$, ** $p < 0.01$, *** $p < 0.001$. **(b)** Dynamic causal modeling (DCM) of rivalry-related changes in effective connectivity. Left: full DCM model. V1 receives eye-specific driving input in replay (green arrow), while all regions (V1, ventral stream, IPS) can receive eye-specific driving input during rivalry (orange arrows). Modulatory effects (orange dots) reflect connectivity differences

between rivalry and replay. Right: group-level parametric empirical Bayes (PEB) analysis reveals enhanced IPS \rightarrow V1 feedback during rivalry compared to replay. No significant modulation was observed for the ventral stream, consistent with the weak amplitudes in (a), suggesting that IPS—not ventral areas—may contribute to modulating interocular competition in V1. DCM inferences identify the best-fitting model within a predefined network architecture and parameter space, and do not imply direct anatomical connections. **(c)** Non-eye-specific switch-related response (aligned to perception switch regardless of dominant eye) in cortical areas. Cross-correlation analysis revealed significant delays in rivalry relative to replay for V1 (1.2 s, 95% CI [0.3, 2.1], $p = 0.017$) and V2 (1.5 s [0.5, 2.8], $p = 0.008$), but not for hV4 (0.4 s [-0.1, 0.9], $p = 0.302$) or IPS (0.1 s [-0.3, 0.5], $p = 0.685$). The V1 delay was also significantly greater than IPS ($p = 0.009$). All p-values were obtained by bootstrapping participants and Holm corrected for multiple comparisons. Shaded bands indicate SEM across 15 participants.



Extended Data Fig. 8 | Ocular-biased clusters in the LGNs for all participants in Exp. 2. Color bars denote t values for the LE-RE contrast of the GLM for localizer runs (two-sided t-statistics; threshold at $\text{abs}(t)>2$; for a few LGNs the threshold was relaxed to 1.5 or 1). Dotted lines mark the anatomical boundaries of the LGN in three coronal slices from anterior (upper panels) to posterior (lower panels).



Extended Data Fig. 9 | Eye-specific responses in the LGN during rivalry and replay. (a) Eye-specific differential response between LE- and RE-biased voxels in the LGN during rivalry (top) and replay (bottom), shown for voxels with the strongest or weakest ocular bias, either inside or outside the ocular-biased clusters. Within OD clusters, voxels were divided by bias strength: “most biased” included the top 100 voxels (50 per eye) with the largest $|LE - RE|$ t-values; “least biased” included the 100 voxels with the smallest $|LE - RE|$ t-values. Voxels can be similarly divided outside the OD clusters but within the anatomical LGN mask, yielding 2x2 conditions in total. With the most biased voxels within OD clusters, rivalry modulation of eye-specific response was negligible (averaged between 4 s and 12 s, LE vs. RE events, $BFO_1 = 3.759$, $n = 15$, two-sided paired Bayesian t-test with default JZS prior), despite robust replay modulation. Least biased voxels

within OD clusters and most biased voxels outside OD clusters showed a negative eye-specific modulation. Line plot: mean value \pm SEM. Gray bars mark time points with significant LE vs. RE differences (FWE $p < 0.05$, cluster-based permutation).

(b) Group-averaged eye-specific response maps (ipsi- vs. contra-lateral eye events) in the LGN. Individual maps were nonlinearly registered to the MNI152 symmetric template. Right LGNs were mirror-flipped and averaged with left LGNs. Coronal slices are displayed anterior to posterior (1.2 mm spacing). Black and white lines outline ipsi- and contra-eye biased clusters from the localizer. The central visual field corresponds to the dorsal and posterior portion of the LGN. The orange dashed line indicates approximately 5 degrees of eccentricity, corresponding to the size of our visual stimuli.

Reporting Summary

Nature Portfolio wishes to improve the reproducibility of the work that we publish. This form provides structure for consistency and transparency in reporting. For further information on Nature Portfolio policies, see our [Editorial Policies](#) and the [Editorial Policy Checklist](#).

Statistics

For all statistical analyses, confirm that the following items are present in the figure legend, table legend, main text, or Methods section.

n/a Confirmed

- The exact sample size (n) for each experimental group/condition, given as a discrete number and unit of measurement
- A statement on whether measurements were taken from distinct samples or whether the same sample was measured repeatedly
- The statistical test(s) used AND whether they are one- or two-sided
Only common tests should be described solely by name; describe more complex techniques in the Methods section.
- A description of all covariates tested
- A description of any assumptions or corrections, such as tests of normality and adjustment for multiple comparisons
- A full description of the statistical parameters including central tendency (e.g. means) or other basic estimates (e.g. regression coefficient) AND variation (e.g. standard deviation) or associated estimates of uncertainty (e.g. confidence intervals)
- For null hypothesis testing, the test statistic (e.g. F , t , r) with confidence intervals, effect sizes, degrees of freedom and P value noted
Give P values as exact values whenever suitable.
- For Bayesian analysis, information on the choice of priors and Markov chain Monte Carlo settings
- For hierarchical and complex designs, identification of the appropriate level for tests and full reporting of outcomes
- Estimates of effect sizes (e.g. Cohen's d , Pearson's r), indicating how they were calculated

Our web collection on [statistics for biologists](#) contains articles on many of the points above.

Software and code

Policy information about [availability of computer code](#)

Data collection	The experiments were programmed in MATLAB v2016b (The Math Works, Inc.) using the Psychophysics Toolbox v3.0.12.
Data analysis	MRI data were analyzed using AFNI v19.0.24 (https://afni.nimh.nih.gov/), FreeSurfer v6.0.0 (https://freesurfer.net/), ANTs v2.2.0 (https://stnava.github.io/ANTs/), mripy package v0.12.13, and the mripy package v0.7.1 developed in our lab (https://github.com/herrlich10/mripy). Effective connectivity of the fMRI data was analyzed with the DCM module of SPM12 (Version 7771). Decoding and clustering analyses were performed using scikit-learn v0.24.2 (https://scikit-learn.org/) and SciPy v1.7.1 (https://scipy.org/). Statistical analyses were conducted using Pingouin v0.5 (https://pingouin-stats.org/), seaborn v0.11.2 (https://seaborn.pydata.org/), JASP v0.14 (https://jasp-stats.org/), R v4.1 (https://www.r-project.org/), and home-built Python code. The mripy package, used in this study for high-resolution fMRI data processing, is available on Github (https://github.com/herrlich10/mripy).

For manuscripts utilizing custom algorithms or software that are central to the research but not yet described in published literature, software must be made available to editors and reviewers. We strongly encourage code deposition in a community repository (e.g. GitHub). See the Nature Portfolio [guidelines for submitting code & software](#) for further information.

Data

Policy information about [availability of data](#)

All manuscripts must include a [data availability statement](#). This statement should provide the following information, where applicable:

- Accession codes, unique identifiers, or web links for publicly available datasets
- A description of any restrictions on data availability
- For clinical datasets or third party data, please ensure that the statement adheres to our [policy](#)

Data to reproduce the main findings of this study can be downloaded from National Basic Science Data Center (<https://www.scidb.cn/en/s/ZJBza>). Raw data can be requested by contacting the corresponding author P.Z. (zhangpeng@ibp.ac.cn).

Research involving human participants, their data, or biological material

Policy information about studies with [human participants or human data](#). See also policy information about [sex, gender \(identity/presentation\), and sexual orientation](#) and [race, ethnicity and racism](#).

Reporting on sex and gender

We recruited participants of both genders (fourteen females and seventeen males in total) for our studies based on their self-reports. Sex or gender effects were not considered because this study focused on understanding the common mechanisms underlying all human beings.

Reporting on race, ethnicity, or other socially relevant groupings

Participants were not grouped by race or ethnicity in the design and analyses of this study.

Population characteristics

Sixteen healthy volunteers (seven females, aged 22–40 years) participated in Experiment 1. Fifteen healthy volunteers (seven females, aged 22–39 years) participated in Experiment 2. All observers had normal or corrected-to-normal vision.

Recruitment

Subjects were experienced psychophysical observers informally recruited from nearby labs based on availability and willingness to participate, without additional screening. Many of them had previous experience with binocular rivalry, but it was unlikely to bias the current results about the general neural mechanisms for the phenomenon.

Ethics oversight

Experimental protocols were approved by the Institutional Review Panel at the Institute of Biophysics, Chinese Academy of Sciences.

Note that full information on the approval of the study protocol must also be provided in the manuscript.

Field-specific reporting

Please select the one below that is the best fit for your research. If you are not sure, read the appropriate sections before making your selection.

Life sciences

Behavioural & social sciences

Ecological, evolutionary & environmental sciences

For a reference copy of the document with all sections, see nature.com/documents/nr-reporting-summary-flat.pdf

Life sciences study design

All studies must disclose on these points even when the disclosure is negative.

Sample size

Sample sizes were determined based on previous works in the literature and the expected effect sizes. Prior human fMRI studies on binocular rivalry typically employed small samples, both for cortical responses (e.g., n = 4 in Polonsky et al., 2000; Tong et al., 2001; n = 3 in Lee et al., 2005; n = 6 in Brascamp et al., 2015) and subcortical responses in the LGN (e.g., n = 4 in Haynes et al., 2005; n = 5 in Wunderlich et al., 2005; n = 3 in Yildirim et al., 2023). In comparison, our final sample sizes of 12 and 15 participants provide substantially greater power, particularly given the enhanced signal-to-noise ratio afforded by 7T fMRI.

Data exclusions

Three subjects were excluded in Experiment 1 due to lack of a clear OD pattern in V1, and one subject was excluded due to strong bias toward one eye. These conditions preclude further OD-specific analyses adopted in this study.

Replication

The reproducibility of ocular dominance columns/clusters identified in V1 (Extended Data Fig. 3d-j) and LGN (Figure 5a/b) were assessed and confirmed by scanning the same subject in different days, and by comparing results from odd and even runs for each individual (Extended Data Fig. 3c). The cortical depth dependent results in V1 were obtained using gradient echo EPI sequence (with T2* weighting and high sensitivity; Figure 2f) in the main experiment, and replicated (in a proof-of-concept case study) using a different pulse sequence (balanced SSFP, with more T2 weighting and better specificity; Figure 2j). The major findings in IPS, including eye-specific modulation during binocular rivalry (Figure 4c/d and Extended Data Fig. 7a) and delayed transition-related response in early visual areas relative to IPS (Figure 4f and Extended Data Fig. 7c) were successfully replicated between Exp.1 and Exp.2. We also showed individual results (Extended Data Fig. 3, 4, 5, 8) to facilitate inspection of replicability between different individuals.

Randomization

We used a within-subject design where all subjects were tested on the same set of experimental conditions, thus randomizing participants to different conditions was not necessary.

Blinding

All participants were exposed to the same experimental conditions. Thus blinding was not necessary.

Reporting for specific materials, systems and methods

We require information from authors about some types of materials, experimental systems and methods used in many studies. Here, indicate whether each material, system or method listed is relevant to your study. If you are not sure if a list item applies to your research, read the appropriate section before selecting a response.

Materials & experimental systems

Materials & experimental systems		Methods	
n/a	Involved in the study	n/a	Involved in the study
<input checked="" type="checkbox"/>	<input type="checkbox"/> Antibodies	<input checked="" type="checkbox"/>	<input type="checkbox"/> ChIP-seq
<input checked="" type="checkbox"/>	<input type="checkbox"/> Eukaryotic cell lines	<input checked="" type="checkbox"/>	<input type="checkbox"/> Flow cytometry
<input checked="" type="checkbox"/>	<input type="checkbox"/> Palaeontology and archaeology	<input type="checkbox"/>	<input checked="" type="checkbox"/> MRI-based neuroimaging
<input checked="" type="checkbox"/>	<input type="checkbox"/> Animals and other organisms		
<input checked="" type="checkbox"/>	<input type="checkbox"/> Clinical data		
<input checked="" type="checkbox"/>	<input type="checkbox"/> Dual use research of concern		
<input checked="" type="checkbox"/>	<input type="checkbox"/> Plants		

Plants

Seed stocks

Report on the source of all seed stocks or other plant material used. If applicable, state the seed stock centre and catalogue number. If plant specimens were collected from the field, describe the collection location, date and sampling procedures.

Novel plant genotypes

Describe the methods by which all novel plant genotypes were produced. This includes those generated by transgenic approaches, gene editing, chemical/radiation-based mutagenesis and hybridization. For transgenic lines, describe the transformation method, the number of independent lines analyzed and the generation upon which experiments were performed. For gene-edited lines, describe the editor used, the endogenous sequence targeted for editing, the targeting guide RNA sequence (if applicable) and how the editor was applied.

Authentication

Describe any authentication procedures for each seed stock used or novel genotype generated. Describe any experiments used to assess the effect of a mutation and, where applicable, how potential secondary effects (e.g. second site T-DNA insertions, mosaicism, off-target gene editing) were examined.

Magnetic resonance imaging

Experimental design

Design type

The localizer task used block design, and the rivalry or replay tasks can be viewed as an event-related design where the events are endogenous.

Design specifications

In Experiment 1 and 2, 4-6 localizer runs were collected for each subject. Each run comprised 12 interleaved monocular stimulation blocks and 2 blank blocks at the beginning and end of the run. Each block lasted 24 s without inter-block interval. 4 rivalry and 4 replay runs, each lasted 256 s, were collected for each subject.

Behavioral performance measures

Mean rivalry interval was 7.13 s for Exp.1 and 7.85 s for Exp.2. No significant difference was found for different eyes or colors (see Extended Data Fig. 1 for mean dominance duration and its confidence interval for each eye and color).

Acquisition

Imaging type(s)

functional, structural

Field strength

7 Tesla

Sequence & imaging parameters

In Experiment 1, T2*w BOLD signals from the occipital and parietal cortices were acquired with a 2D GE-EPI sequence (0.8 mm isotropic voxels, 31 oblique-coronal slices, FOV = 128×128 mm, TE = 23 ms, TR = 2000 ms, nominal flip angle = 80°, bandwidth = 1157 Hz/pixel, partial Fourier = 6/8, GRAPPA = 3). One subject was also scanned with a 2D passband balanced SSFP sequence to acquire T2w BOLD signals (voxel size 0.5 × 0.5 × 1.5 mm, 2 oblique-coronal slices, FOV = 96 × 96 mm, volume acquisition time = 2400 ms for localizer and 1600 ms for rivalry/replay, TR = 5.64 ms, TE = 2.82 ms, nominal flip angle = 29° or 30°, bandwidth = 521 Hz/pix, no in-plane acceleration for localizer and GRAPPA = 2 for rivalry/replay). 3D passband bSSFP sequence (0.8-mm isotropic voxels, 10 oblique-coronal slices, FOV = 102 × 102 mm, volume acquisition time = 6 s, TR = 5.54 ms, TE = 2.77 ms, nominal flip angle = 15°, bandwidth = 471 Hz/pix, partial Fourier = 7/8 in both phase and slice direction, GRAPPA = 2) was also used in a separate localizer session to evaluate the robustness of V1 ODC pattern.

The same 2D GE-EPI sequence was used, albeit with different parameters in Experiment 2 (1.2 mm isotropic voxels, FOV = 180×180 mm, TE = 22 ms, flip angle = 78°, bandwidth = 1587 Hz/pix, GRAPPA = 2. 62 oblique-transversal slices were acquired for 8 of 15 subjects with a multi-band factor of 2. 31 slices were acquired for the rest of subjects without

multi-band acquisition). EPI volumes with reversed phase encoding and readout directions were also acquired for susceptibility distortion correction.

For all Experiments, T1w anatomical volumes were acquired using a MP2RAGE sequence (0.7 mm isotropic voxels, FOV = 224x224 mm, 256 sagittal slices, TE = 3.05 ms, TR = 4000 ms, TI1 = 750 ms, flip angle = 4°, TI2 = 2500 ms, flip angle = 5°, bandwidth = 240 Hz/pix, partial Fourier = 7/8, GRAPPA = 3).

Area of acquisition

Diffusion MRI

Used

Not used

Preprocessing

Preprocessing software

MRI data were preprocessed using AFNI (v19.0.24), FreeSurfer (v6.0.0), ANTs (v2.2.0), and the mripy package developed in our lab (<https://github.com/herrlich10/mripy>). EPI volumes were corrected for slice timing, susceptibility distortion (blip-up/down method), head motion (6 parameters rigid body), and rescaled to percent signal change. To minimize the loss of spatial resolution, all spatial transformations were combined and applied in a single interpolation step (sinc method), in which the data were also up-sampled by a factor of 2. The anatomical volumes were segmented and reconstructed into surfaces using the default FreeSurfer pipeline (recon-all with -hires option for submillimeter T1 volumes). The surfaces were visually inspected and manually edited, mainly to remove dura mater and sinuses from the gray matter. The T1 volume and the surface were aligned to the mean of preprocessed EPI images (cost function: ipc). Relative cortical depth (0-1) for each voxel was estimated using an equivolume method (mripy_compute_depth.ipynb in mripy). To match the up-sampled volume grid and alleviate the vertex-missing problem during surface-to-volume projection, high density surface meshes were created (mripy_create_hd_mesh.ipynb).

Normalization

The fMRI data were analyzed in the native space of individual subjects to exploit the submillimeter spatial resolution. The ODC pattern in V1 is unique for each subject and defies spatial normalization.

Normalization template

The data were not normalized.

Noise and artifact removal

Motion correction parameters were included as regressors of no interest in the GLM analysis.

Volume censoring

A volume would be censored if the derivative of head motion parameters has a Euclidean norm greater than 0.3.

Statistical modeling & inference

Model type and settings

For the eye-preference localizer, mass univariate regression analysis was conducted at the first-level using the Block4 HRF in AFNI. Slow drift in the signal was modeled using Legendre polynomials of an automatically determined order (3dDeconvolve -polort 'A'). Head motion parameters were included as nuisance regressors. Temporal autocorrelation was accounted for using a ARMA(1,1) model (3dREMLfit). At the second level, subject was treated as a random effect, and experimental manipulation (rivalry vs replay) and different layers or ROIs as fixed effects. For rivalry and replay condition, both event-related averaging and deconvolution analysis (3dDeconvolve with CSPLINzero model in AFNI) were used.

Effect(s) tested

For eye-specific response modulation, the main dependent variable is the difference in BOLD response when the subjects report seeing the left eye image vs seeing the right eye image. For synchrony across visual field, the dependent variable is the width of r-value distribution for moment-to-moment correlation between V1 activation pattern and its ODC map. The main effect of interest is rivalry vs replay, and cortical layers (deep, middle, superficial). Repeated measures ANOVA was used for hypothesis testing, followed by paired t-tests.

Specify type of analysis: Whole brain ROI-based Both

Anatomical location(s)

In Experiment 1, V1 ROIs were manually drawn on the cortical surface to select regions with a clear and roughly balanced pattern of ODCs (see Extended Data Fig. 3a for the OD patterns and ROIs of all subjects). Vertices with significant ocular bias (LE-RE contrast abs(t) > 2) and visual response (LE+RE t > 2) were then projected to the volume space to select voxels in a column-wise manner. IPS was defined as the union of IPS0 to IPS5 in Wang15 atlas (Wang et al., 2015), whose masks were generated using the neuropthy package (Benson et al., 2018). pIPS and aIPS was defined as IPS0-2 and IPS3-5, respectively. In Experiment 2, anatomical mask for each LGN was manually delineated in the T1w volume, and two clusters of voxels with significant ocular bias (LE-RE abs(t) > 2; for a few LGNs the threshold was relaxed to 1.5 or 1) were identified for each LGN (Extended Data Fig. 8 shows the ocular biased clusters for all subjects). V1 voxels with significant ocular bias (LE-RE abs(t) > 2) and positive visual response (LE+RE > 0) were included for ROI analysis.

Statistic type for inference

(See [Eklund et al. 2016](#))

We performed ROI-based analyses and ROIs were selected using independent functional localizers and anatomical information.

Correction

Holm correction were used for multiple comparisons across ROIs and conditions when needed.

Models & analysis

n/a Involved in the study

Functional and/or effective connectivity

Graph analysis

Multivariate modeling or predictive analysis

Functional and/or effective connectivity

Effective connectivity of the fMRI data was analyzed with the DCM module of SPM12 (Version 7771). Multivariate decoding timeseries from V1, V2, and IPS were used as VOI inputs. The model (Fig. 4e inset) had two inputs: the eye-of-origin of the currently perceived stimulus (high for LE and low for RE) was defined as a driving input to V1 in the replay condition, while all brain areas (V1/V2/IPS) could receive such an eye-specific driving input during rivalry. Fixed connections were defined between and within all brain areas, and the between-areas connections were allowed to be modulated by the 2nd input during binocular rivalry. Both inputs were mean-centered. A bilinear, single state, deterministic model with default parameters was used. At the first level, the full DCM for each subject was estimated using all data from rivalry and replay runs concatenated together. At the second level, we used the parametric empirical Bayes method to perform Bayesian model reduction, Bayesian model average, and make inferences about the connectivity strength. Default parameters and priors were used during model fitting.

Multivariate modeling and predictive analysis

To obtain a single real number that best predicts which eye is stimulated based on the activation pattern in a given ROI, a set of linear weights can be learned by training a linear classifier (we used linear support vector machines from the scikit-learn package with default hyper-parameters) on ocular bias localizer data to predict which eye was stimulated on a TR-by-TR basis, and the multivariate response patterns from other conditions can then be linearly projected using the optimal weights into a 1D timeseries that reflects the distance to the decision boundary at each moment. This decoding timeseries is the multivariate differential response, and can be used to compute an event-related average response. For feature selection, voxels with above-threshold visual response (omnibus $F > 1$, $L+R t > 1$, $L+R \beta < 5$) and ocular bias (200 most biased voxels (2x up-sampled) in both ends of the L-R t distribution, with positive monocular response, e.g., LE > 0 for LE-biased voxels) in the GLM results of ocular bias localizer were selected. Results were similar across a reasonable range of thresholds. The ideal response timecourse for the localizer was created by convolving the HRF ("GAM" with default parameters in AFNI) with boxcar functions indicating LE or RE blocks, and then taking their difference. Volumes at the flat part of the block responses (absolute value of the ideal response $> 0.75 * \text{maximum}$) were selected for training, whereas all volumes from the rivalry/replay runs were used at test time for generating the multivariate differential response. Each sample (feature vector) was normalized to have unitary Euclidean norm before training or testing.